CHALMERS
UNIVERSITY OF TECHNOLOGY

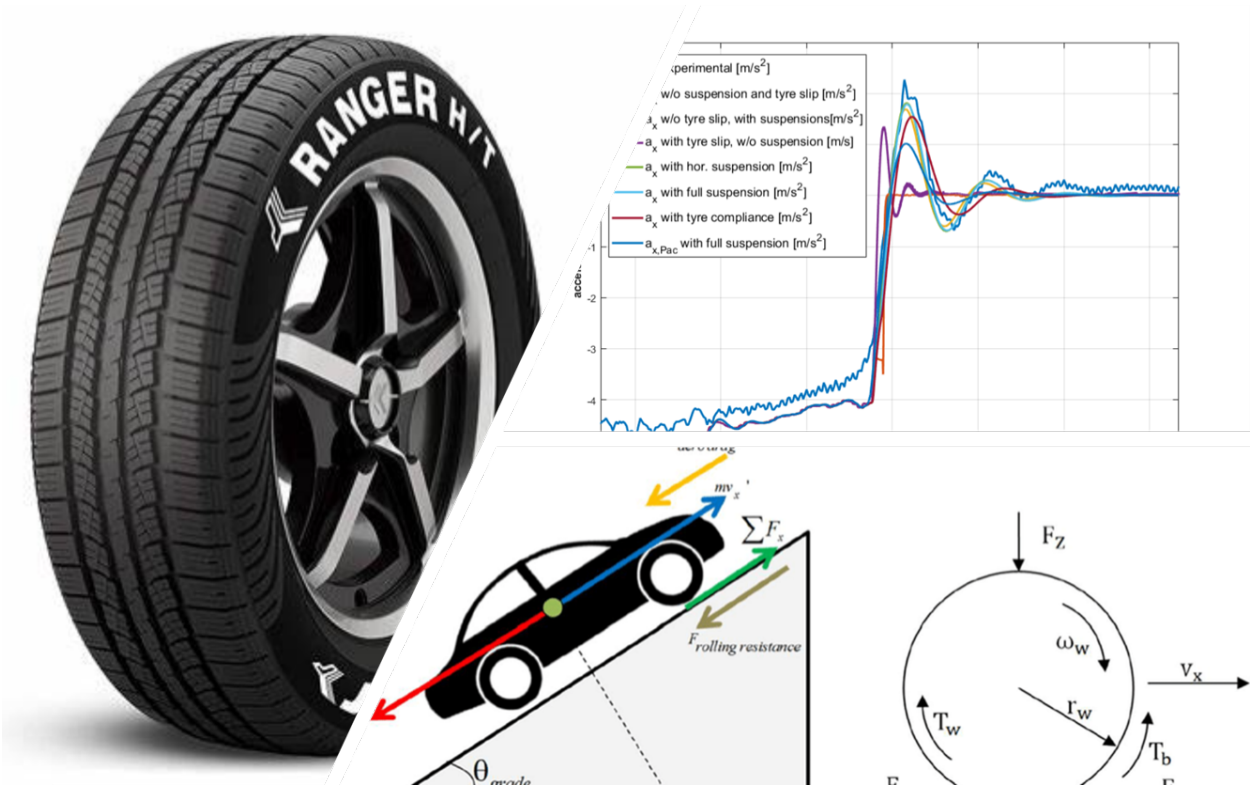

Modelling of longitudinal vehicle motion during low-speed driving

LUCA MEREU

DEPARTMENT OF MECHANICS AND MARITIME SCIENCES

CHALMERS UNIVERSITY OF TECHNOLOGY
Gothenburg, Sweden 2023
www.chalmers.se

Master's thesis in Automotive Engineering

Modelling of longitudinal vehicle motion during low-speed driving

LUCA MEREU

CHALMERS
UNIVERSITY OF TECHNOLOGY

Department of Mechanics and Maritime Sciences
Divisions of Vehicle Engineering and Autonomous Systems
Chalmers University of Technology
Gothenburg, Sweden 2023

Modelling of longitudinal vehicle motion during
low-speed driving
LUCA MEREU

Supervisor: Mats Jonasson, Division of Vehicle Engineering and Autonomous Systems, M2
Examiner: Petri Piiroinen, Division of Dynamics, M2

Master's Thesis 2023
Department of of Mechanics and Maritime Sciences
Divisions of Vehicle Engineering and Autonomous Systems
Chalmers University of Technology
SE-412 96 Gothenburg
Telephone +46 31 772 1000

Cover: Modelling of longitudinal vehicle motion during low-speed driving.

Typeset in LaTeX
Printed by Chalmers Reproservice
Gothenburg, Sweden 2023

Modelling of longitudinal vehicle motion during
low-speed driving.
LUCA MEREU
Department of Mechanics and Maritime Sciences
Chalmers University of Technology

Abstract

The phenomenon of sudden jolts when riding in a vehicle is a well-known phenomenon which is caused by friction forces between the ground, tyres, disc-brake systems and suspensions. It is caused by two significant nonlinear singularities, which arise from friction forces between the ground and the tyres as well as within the disc-brake system. The jerk phenomenon occurs due to the frictional forces between two surfaces when there is a change in the direction of their relative velocity.

In this thesis, some of the most common friction models will be investigated. Simulations are performed to evaluate the limits and the performances of the different models applied to a brake disc. Additionally, a novel tyre model based on the LuGre friction model is implemented to address singularities at low speeds. A comparison is made between this new model and the widely recognized Pacejka tyre model to highlight the differences and the limits of each. Furthermore, a complete longitudinal vehicle model featuring these tyre and brake models is developed. Different complexities of the model are considered, ranging from a complete rigid vehicle model to models featuring suspensions and compliances. This will allow us to gain knowledge of where the jerk phenomenon arises. To validate the model, the mathematical results are compared with experimental data obtained from actual vehicle manoeuvres.

List of Acronyms

Below is the list of acronyms that have been used throughout this thesis listed in alphabetical order:

ADAS	Advanced driver-assistance system
DOF	Degrees of freedom
FBD	Free-body diagram
GoG	Centre of gravity
IMU	Inertia Measurement Unit
RMS	Root mean square
RMSE	Root mean square error

Nomenclature

In the following the list of names and terms for indices, parameters and variables used in the equations and mathematical-physical expressions of this thesis.

Parameters

Parameter	Unit of measure	Description
B	[N/-]	Pacejka slip stiffness parameters
C	[-]	Pacejka shape parameters
c_{belt}	[Nm/rad]	Tyre sidewall stiffness
d_{belt}	[Nm/rad]	Tyre sidewall damping
$c_{sus,h}$	[N/m]	Suspension attachment compliance stiffness
$d_{sus,h}$	[Ns/m]	Suspension attachment compliance damping
$c_{sus,i}$	[N/m]	Suspension stiffness
$d_{sus,i}$	[Ns/m]	Suspension damping
C_x	[N/-]	Tyre longitudinal stiffness
D	[N]	Pacejka peak force parameters
E	[-]	Pacejka curvature parameters
F_d	[N]	Dynamic friction force
F_N	[N]	Normal force
F_s	[N]	Static friction force
F_t	[N]	Tangential force
F_x	[N]	Longitudinal force
F_z	[N]	Vertical force
G	[Pa]	Tyre rubber shear stress modulus
H	[m]	Contact patch Height
i	[-]	Counter

J	[kgm^2]	Inertia
L	[m]	Contact patch length
m	[kg]	Mass
N	[-]	Number of bristle
p	[Pa]	Pressure
R	[m]	Radius
R_m	[m]	Mean brake pad radius
R_p	[m]	Brake cylinder radius
s_x	[-]	Tyre longitudinal slip
t	[s]	Time
T	[Nm]	Torque
v_r	[m/s]	Relative velocity
v_s	[m/s]	Stribeck velocity
v_x	[m/s]	Longitudinal velocity
W	[m]	Contact patch width
x	[m]	Longitudinal position
$\dot{x}$, v, V	[m/s]	Longitudinal velocity
$\ddot{x}$, $\dot{v}$ or $\dot{V}$	[m/s^2]	Longitudinal acceleration
z	[m]	Bristle displacement
$\dot{z}$	[m/s]	Bristle velocity
α	[rad]	Slope angle
α_i	[-]	Shape friction factor
γ	[rad]	Bristle deflection angle
θ	[rad]	Rotation angle
μ_d	[-]	Dynamic friction coefficient
μ_s	[-]	Static friction coefficient
ξ	[m]	Contact patch coordinate
σ_0	[N/m]	Stiffness
σ_1	[Ns/m]	Micro-damping
σ_2	[Ns/m]	Viscous damping
ω	[rad/s]	Angular velocity
$\dot{\omega}$	[rad/s^2]	Angular acceleration

Contents

List of Figures

List of Tables

Preface

Thanks to technological advancement in the field of autonomous vehicles, it will become more and more important to ensure that people who use this technology feel safe and comfortable being on the move.

Unpleasant sudden jolts when being in a vehicle that is either starting or coming to a stop can be experienced. One common issue that can arise during vehicle acceleration or deceleration is the presence of sudden and unpleasant jolts caused by two significant nonlinear singularities. These singularities stem from friction forces between the ground and the tyres as well as within the disc-brake system. Moreover, when the relative velocity between two touching objects approaches zero, there can be numerical issues in estimating the slip condition of the tyres. This is particularly challenging as proper slip estimation is necessary to ensure accurate control actions. In addition, at low speeds, the jerk phenomenon can also make it challenging to measure motion states, such as wheel speed and torque.

All these issues must be properly measured and accounted for by the vehicle control unit to smooth as much as possible rapid changes in acceleration to give passengers the best experience possible.

Luca Mereu, Gothenburg, June 2023

Chapter 1

Introduction

There are two phenomena that need to be carefully monitored in the context of advanced driver-assistance systems (ADAS) and autonomous driving:

1. Mechanical friction.
2. Tyre slip estimation and velocity estimation.

Accurately assessing the impact of friction and the tyre slip state can enhance passenger safety and riding comfort by enabling improved control measures. The following sections will provide a brief explanation of the friction phenomena, tyre slip and their connection with jerk, to gain a better understanding of the issues involved.

1.1 Mechanical friction

Generally, during the simulation of mechanical dynamic systems, relatively straightforward mathematical models (e.g. Coulomb-based models) can be used to estimate the effect of friction forces under specified scenarios when the relative position between objects is not important. However, when a robust control strategy is needed, it becomes necessary to have a model that is able to determine the phenomenon of friction at low speeds and when the speed approaches zero.

Let us consider the example of a simple mass of 70 kg moving down a plane inclined at an angle α (see Figure 1.1). With the longitudinal coordinate of the plane denoted as x, we will use the notations $\dot{x}$ and $\ddot{x}$ to represent the speed and acceleration of the mass, respectively. The forces acting on the mass include the gravitational force, the normal force from the plane reaction to the weight of the mass, and the tangential force resulting from friction. Here we let the mass initially move with the speed $\dot{x} = 2$ [m/s] with $\alpha = 15$ [°]. The dynamic equations of the system are given by (1.1):

$$m \cdot g \cdot \sin(\alpha) - F_f = m \cdot \ddot{x}, \tag{1.1a}$$

$$m \cdot g \cdot \cos(\alpha) - F_N = 0, \tag{1.1b}$$

where F_f represents the friction force modelled with the classic Coulomb model (see Figure 1.1 right) so that

$$F_f = \begin{cases} F_s, & \dot{x} = 0, \\ -F_d \cdot \text{sign}(\dot{x}), & \dot{x} \neq 0. \end{cases} \tag{1.2}$$

Essentially, the model produces a dynamic friction force F_d in the presence of motion and a static force F_s when at zero speed. The Coulomb friction is used as an approximation to calculate this force and is defined by the equations (1.3) and (1.4). The first equation calculates the static force, where the velocity is zero, using the static friction coefficient μ_s and the normal reaction force F_N. The second equation calculates the dynamic force, where the velocity is non-zero, using the dynamic friction coefficient μ_d and the normal reaction force.

$$F_s = \mu_s \cdot F_N, \tag{1.3}$$

$$F_d = \mu_d \cdot F_N. \tag{1.4}$$

The friction force is then represented proportionally to the normal load with the friction coefficient defining the relationship between these two forces. The static friction force is the exact amount needed to prevent motion between the surfaces, balancing the net force that could cause motion. The Coulomb approximation sets a threshold for this force, above which motion would occur, rather than providing an exact value for the friction force.

Analyzing the system depicted in (Figure 1.1) the mass is expected to come to a stop, decelerated by the friction force, and to reach the steady-state value $m \cdot g \cdot \sin(\alpha)$, as the acceleration $\ddot{x}$ also approaches zero. However, in the context of numerical simulations, it is not always clear how the static friction force will behave, since only the threshold $\pm\mu_s \cdot F_N$ is defined (see Figure 1.1 (right)).

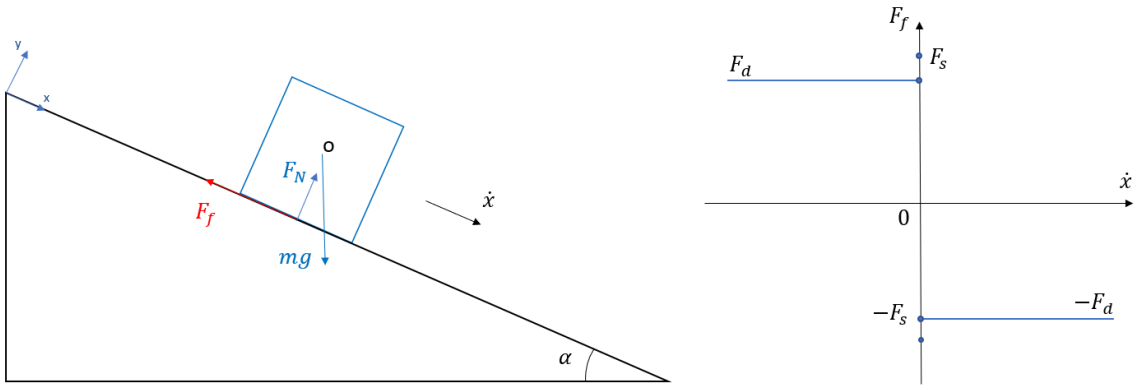

Figure 1.1: A mass moving down an inclined plane (left) and the Coulomb friction model used (right).

If using such a simple friction model in the numerical domain, when simulating the system in software (Simulink© in such case), as the mass speed $\dot{x}$ decreases, what

happens is that the friction force starts to oscillate between F_d and $-F_d$ (Figure 1.2). These oscillations occur because the simulation never reaches $\dot{x} = 0$ due to the use of a fixed time-step solver. Consequently, the friction force assumes always the dynamic force defined for $\dot{x} \neq 0$. However, since the simulation is running on Simulink©, where the sign function is defined as

$$\text{sign}(\dot{x}) = \begin{cases} 1, & \dot{x} > 0, \\ 0, & \dot{x} = 0, \\ -1, & \dot{x} < 0, \end{cases} \tag{1.5}$$

if $|F_d|$ is higher than the gravitational force acting on the plane, as $\dot{x} = 0$ is crossed, the friction begins to act in the opposite direction to the motion and reverses it. In this scenario, the friction becomes equal to $-F_d$, and the cycle repeats. However, it is important to note that this is unphysical since friction is a dissipative force and it can not generate motion.

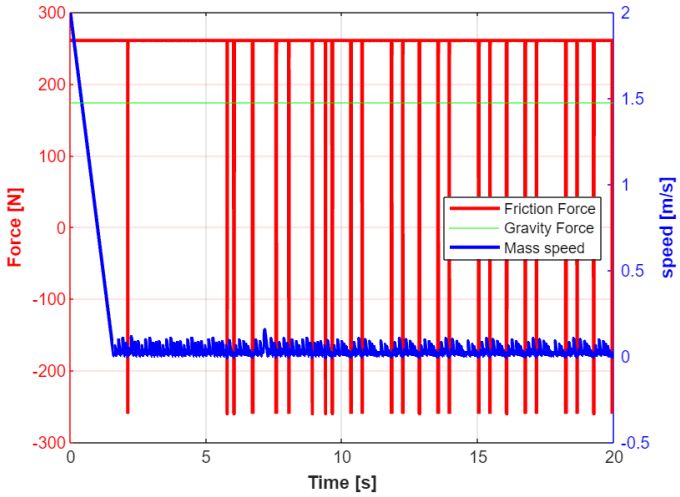

Figure 1.2: Friction force (red) and speed (blue) for the mass described in Section 1.1.

When working with simulation software, it becomes important to describe the friction phenomenon even when the relative motion between two surfaces is zero. A precise understanding of friction forces at zero speed can enhance the effectiveness of simulation tools, allowing for more accurate predictions of system behaviour.

1.2 Tyre slip

The tyre-force model plays a crucial role in vehicle dynamics simulations. Due to the involvement of composite materials and the contact with the road surface, the tyre-force characteristic exhibits significant non-linearity [8]. Usually, for normal driving conditions, experimental tyre modelling can be used to estimate the tractive or braking force that a tyre can generate as a function of the tyre slip (Figure 1.4).

Tyre slip refers to the *normalized* difference between the rotational speed of the

tyre and its longitudinal speed, see (1.6). When the tyre slip increases, the tyre contact points with the ground move relative to the ground itself, introducing shear stresses that produce the tyre-ground force. With reference to Figure 1.3 it can be demonstrated [7] that a proper definition of the tyre slip ratio is

$$s = \frac{\omega \cdot R - V}{|\omega \cdot R|}. \tag{1.6}$$

However, it can be noticed that when the angular speed approaches zero, also the denominator approaches zero and numerical problems can occur. During braking phases, the angular speed becomes zero before the longitudinal one (as the slip ratio must be negative to generate a negative force that can brake the wheel).To overcome this issue, in the literature ([8, 15]), the slip is then modified to

$$s = \frac{\omega \cdot R - V}{|V|}. \tag{1.7}$$

This alternative definition enhanced stability during braking manoeuvres. On the other hand, during acceleration phases, the angular speed rises earlier than the longitudinal one (since the slip ratio must be positive to generate a tractive force that can accelerate the wheel). Thus, (1.6) is preferred in such cases.

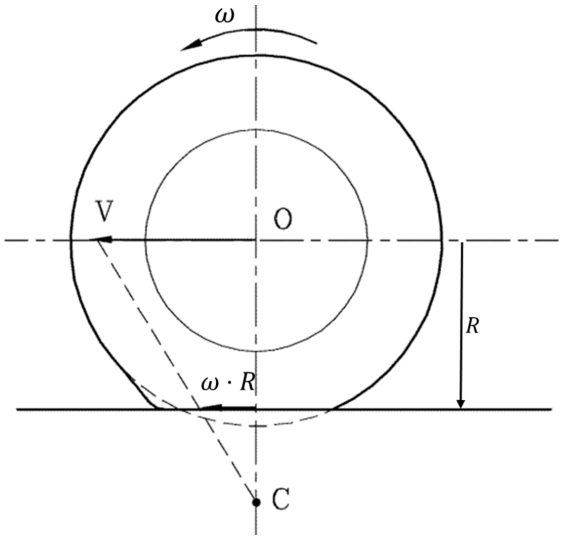

Figure 1.3: Tyre moving at the velocity V and with an angular velocity ω. R represents the tyre rolling radius, while C corresponds to the instant centre of rotation of the wheel. The normalized difference between the wheel centre speed V and tyre tread speed $\omega \cdot R$ is referred to as slip. This slip is what makes the tyre able to produce a longitudinal force on the ground [13].

However, the magnitude and the direction of this force depend also on other factors, such as tyre load and road surface characteristics. The friction between the tyre and the ground generates a tyre-ground force, with the amount of force increasing with the magnitude of the tyre slip. However, beyond a certain point, the tyre slip can lead to a decrease in the tyre-ground force due to friction saturation. Therefore, understanding the effect of tyre slip on tyre-ground force generation is crucial for predicting and controlling the motion of a vehicle.

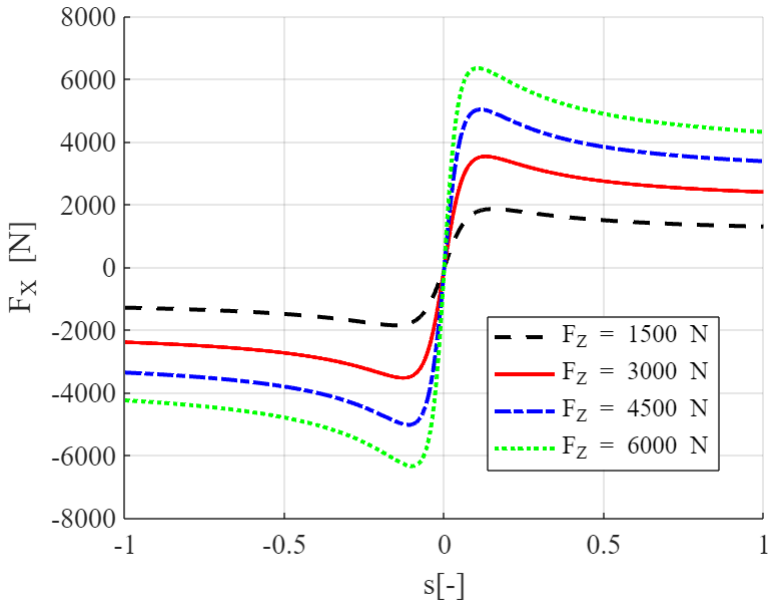

Figure 1.4: An example of tyre force F_x vs. slip characteristics of a tyre. It demonstrates the impact of the normal load on the generated force as well as the behaviour of the force concerning the slip of the tyre.

1.3 Jerk phenomenon

Despite the problems previously mentioned when simulating real-world effects, once they are solved, we want to estimate the so-called *jerk* effect. Looking at a more realistic friction graph (Figure 1.5) it can be seen that when approaching zero speed, the friction force increases quickly to pass from F_d to F_s. Let us consider a wheel being decelerated by a disc brake (Figure 1.6) and attempt to model the friction between the brake pads and disc while maintaining a constant braking pressure. It can be observed that, as the disc approaches zero speed, the friction force rises (in Figure 1.5, see the trend inside the red circle) and so does the acceleration (*jerk* effect highlighted in Figure 1.7). Look at the acceleration peak when the wheel stops moving [14]). This is what creates the uncomfortable behaviour discussed in the Preface.

This phenomenon is not limited to the example of a brake pad. For instance, consider a person inside a vehicle who is travelling at a constant speed and who suddenly applies hard braking pressure. In this case, since the slip between the tyre and the ground can be described by (1.7), as the rotational speed of the tyre decreases, the slip will increase. Referring to Figure 1.4, the increased slip will result in a corresponding increase in braking force and acceleration.

1.4 Preliminary aims

The aims of the thesis is to address the problems caused by singularities and to model them so they can accurately describe real-world physics. It is then possible

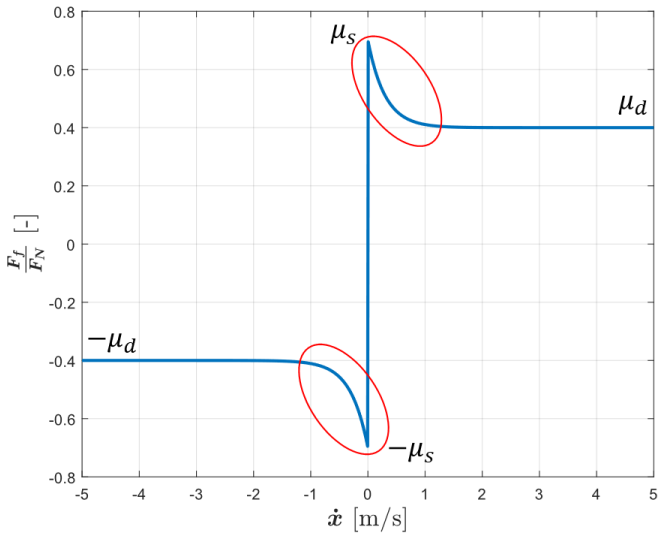

Figure 1.5: Friction force behaviour that is more representative of the real physic effect than the classic Coulomb model (Benson model 2.2). As the speed reduces, the friction force increases exponentially to pass from F_d to F_s.

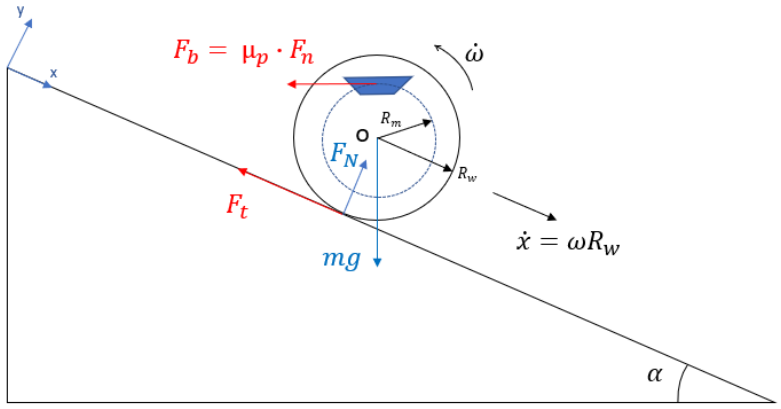

Figure 1.6: Wheel equipped with a disc brake that is braking it to stop the motion.

to identify the following area of research:

- Quantify vehicle safety and comfort issues: Analyse the singularities that can lead to safety hazards and discomfort for the driver and passengers.
- Develop mechanical and mathematical models: Develop mathematical and mechanical models that represent a vehicle behaviour in the presence of singularities. The use of software like MATLAB©/Simulink© will be leveraged to numerically show the results.
- Numerical analysis of the models: The models that have been developed will be used to perform numerical simulations, aimed at assessing the impact of singularities on vehicle dynamics. It is crucial to carefully select the appropriate parameters, such as the numerical solver and time step, to prevent any loss of critical information. Since jerk occurs within a very narrow time frame, it

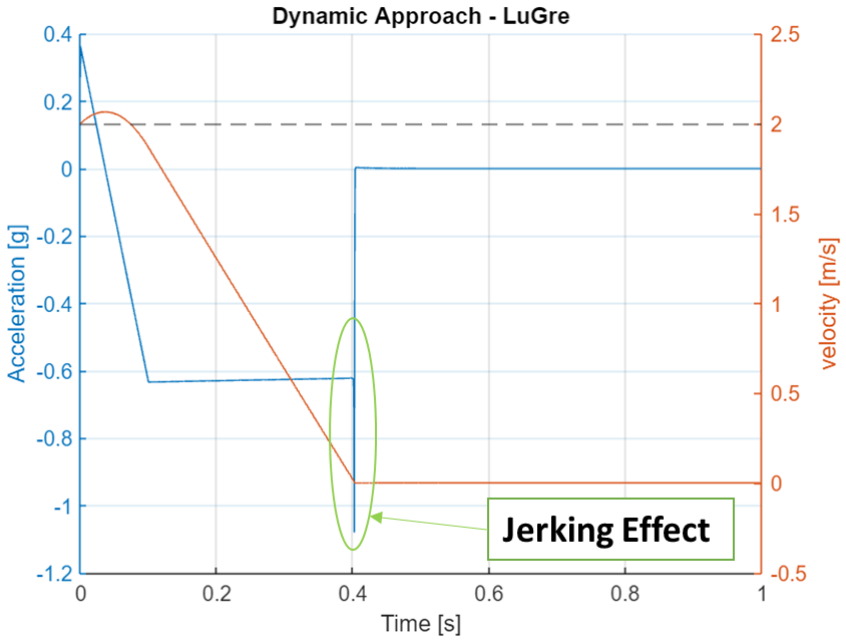

Figure 1.7: Longitudinal acceleration (blue curve) and speed graphs (orange curve) of a wheel decelerated by a disc brake.

is essential to select a suitable time step that can accurately capture the *true* acceleration peaks and not only the trends.

- Verification through experiments: To validate the developed models, experiments can be conducted using real vehicles model under controlled conditions. The results from these experiments can then be compared with the predictions made by the developed models to tune and validate them.

By following these steps, it is possible to gain a better understanding of the effects of singularities on vehicle dynamics, develop models that accurately predict these effects, and devise strategies to mitigate the associated safety and comfort problems with the optics of autonomous driving.

1.5 Hypothesis and constraints

Since it is not feasible to use models with dozens of degrees of freedom when simulating vehicles with many wheels, the work will be carried out under the following assumptions:

- Only the longitudinal dynamics of vehicles will be considered.
- All simulations will be carried out without considering vibrations coming from engines or motors.
- The road and surfaces are considered smooth (no noise and vibration harshness are considered).
- The compliance and stiffness of components such as brake clamps and transmission shafts will not be taken into consideration.

1.6 Objective

The main goal of the thesis is to:

- Mathematically describe how friction behaves at each possible speed v (from high speed to 0 speed) through

$$F_f = \mu(v) \cdot N, \quad \forall v,$$

where

$$\begin{aligned} &\mu(v) \text{ is the friction coefficient varying with the speed and} \\ &N \text{ is the normal force acting on the sliding surfaces.} \end{aligned} \tag{1.8}$$

- Formulate a model that is able to describe how tyres produce force even when information from the original slip formulation becomes unphysical.
- Identify and measure where jerk emanates and its effect on vehicle longitudinal acceleration.
- Describe and show how friction and tyre models interact with each other.
- Verify the derived models using measurements from model experiments.
- Develop a control strategy to minimize jerk effects (e.g. a controller that reduces brake pressure as speed approaches zero).

Chapter 2

Friction models

Describing the phenomena of friction when the relative speed between bodies is zero can be a challenging task. To this end, numerous friction models have been developed over the years, which aim to provide an accurate representation of how forces are exchanged in static conditions. In this section, we will provide an overview of the most common friction models used in the field of dynamic systems [14]. It can be noted that the friction models based on analytic expressions can generally be categorized into two main groups. The first group includes models that rely on Coulomb friction law, which provides a simple yet effective way of modelling friction forces between two surfaces in contact. The second category consists of more intricate models that describe the contact behaviour as interaction between bristles, rather than flat surfaces.

2.1 Coulomb based models

The Coulomb friction models aim to describe the friction behaviour between two surfaces in a simple yet effective manner. The model assumes that the surfaces are flat and that the interaction between them is determined by a coefficient of friction, which aims to capture the fundamental properties of friction. From a mathematical point of view, the friction force, tangent to the surfaces in contact, is analytically expressed as [14]

$$F_f = \begin{cases} [-\mu_s \cdot F_N, \quad \mu_s \cdot F_N], & v = 0, \\ -\mu_d \cdot F_N \cdot \operatorname{sgn}(v), & v \neq 0. \end{cases} \tag{2.1}$$

Where

μ_s is the static friction coefficient, μ_d is the dynamic friction coefficient and F_N is the normal force acting on the sliding surfaces.

As shown in Figure 2.1, when the relative speed between the surfaces is greater than zero, the dynamic friction acts in the opposite direction to the motion and remains constant. However, when the speed decreases to zero, the friction suddenly goes to the static value. It is important to note that this model does not provide a clear description of what happens when the sum of the external forces is less than the

static friction force (at $v = 0$). Furthermore, this model is not taking into account the viscous phenomenon which tends to increase the amount of friction at high speeds.

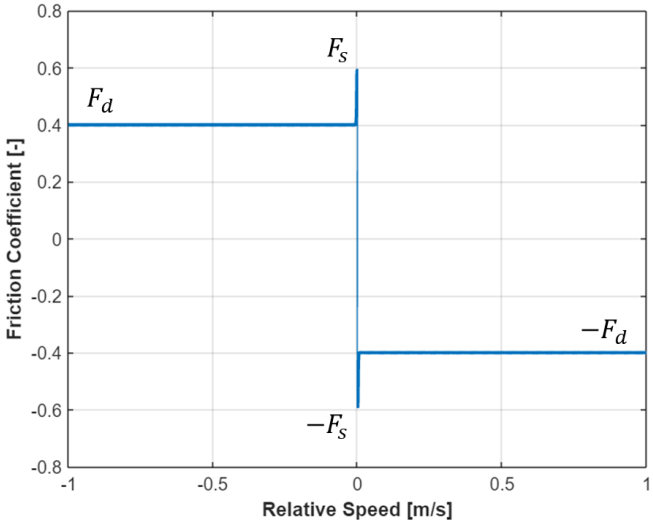

Figure 2.1: Classic Coulomb Model.

Efforts have been made to enhance the precision of the classic Coulomb model. In fact, since mechanical contacts involve bodies compliance, the friction force cannot experience an abrupt transition (from F_s to F_d) [14]. To account for this, Figure 2.2 shows the representation of the so-called Benson model where the shift from static to dynamic condition is modelled with an exponential function such that

$$F_f = \begin{cases} [-\mu_s \cdot F_N, \quad \mu_s \cdot F_N], & v = 0, \\ -\left(\mu_d + (\mu_s - \mu_d) \cdot e^{-(\frac{v}{v_s})^{\alpha}}\right) \cdot F_N, & v \neq 0, \end{cases} \tag{2.2}$$

where v_s is the Stribeck velocity which represents an exponential decay constant. As shown in Figure 2.2, In contrast to the conventional Coulomb model, the dynamic friction of the system exponentially approaches the static value as the velocity decreases to zero. However, it is important to note that a comprehensive explanation of what occurs when the sum of the external forces is less than the peak static friction force is not provided either with this formulation.

As already mentioned, the previous models cannot really capture what happens when the speed is zero. For simple mechanical systems where friction does not play an important role, models such as the velocity-based friction model can be used. In this context, a different formulation is introduced to emulate the phenomenon of stiction. In particular within a narrow interval that includes zero velocity [14], the friction force shape is not vertical as for the previous formulations, but a small velocity is allowed to ensure the continuity of the model when the static force is the interval $[-F_s, F_s]$. The model can be formulated as

$$F_f = -\mu_s \cdot \sin\left[C \cdot \arctan\left(B \cdot v\right) - E \cdot \left[(B \cdot v) - \arctan\left(B \cdot v\right)\right]\right] \cdot F_N \tag{2.3}$$

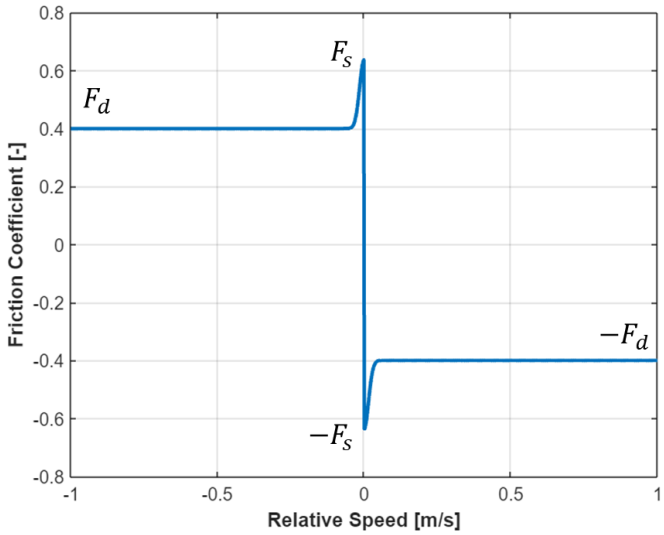

Figure 2.2: Benson Model representation.

This function makes use of the parameters C, B, and E, to change the shape of the curve to enable it to accurately match experimental data [14] (see Figure 2.3 for its representation).

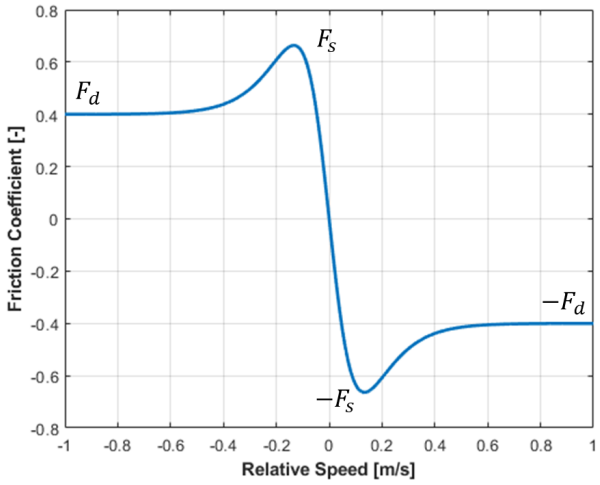

Figure 2.3: Velocity-based friction model.

2.2 Bristle models

Additional models can be developed to incorporate the effect of viscous contact, but the crucial issue is the implementation of the stiction phase. Bristle models take this into consideration and aim to replicate the physics of micro-scale structures where the surface roughness is then modelled like bristles (see Figure 2.4). Here a brief review of the most common Bristle models presently used will be given.

Bristle friction models are based on the fundamental principle that when two surfaces with bristles come into contact, the bristles on one surface interlock with those on the other surface (see Figure 2.4), generating friction forces that resist the relative motion between the two surfaces. This interlocking mechanism can be mathematically modelled as a parallel connection of a spring and a damper, with the specific values of these parameters varying depending on the material properties of the surface in contact [6].

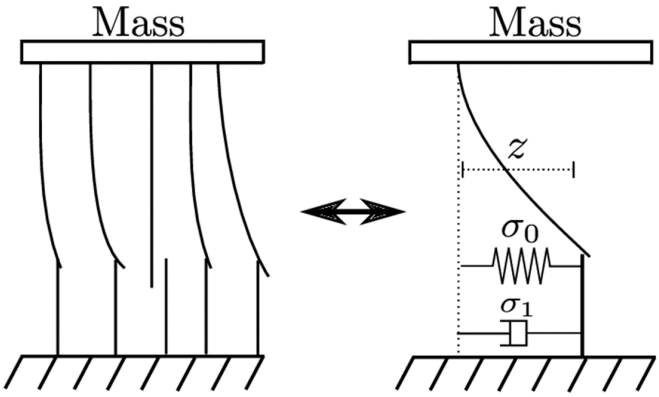

Figure 2.4: Bristle model [6].

2.2.1 LuGre model

In the LuGre[1] model, the friction force is thought as a function of the mentioned stiffness and damping and is given by

$$F_f = \sigma_0 \cdot z + \sigma_1 \cdot \dot{z} + \sigma_2 \cdot \dot{v}, \tag{2.4}$$

where σ_0 and σ_1 are the stiffness and the damping of the bristles, respectively, while σ_2 denotes the viscous damping effect of lubricated systems [14]. The variable z is used as a state variable to describe the average deflection of all the bristles, and can be mathematically expressed as

$$\dot{z} = v - \sigma_0 \cdot \frac{|v|}{g(v)} \cdot z. \tag{2.5}$$

The function *g(v)* represents a force that varies with velocity and is capable of replicating both the Coulomb friction and the Stribeck effect (the exponential decay to move from F_s to F_d) [14]. The function is given by

$$g(v) = F_d + (F_s - F_d) \cdot e^{-\left(\frac{v}{v_s}\right)^{\alpha}}, \tag{2.6}$$

where both v_s (Stribeck velocity) and α are parameters that aim to shape the Stribeck effect itself.

[1] Named to recognize that it originated in a collaboration between the control groups in Lund and Grenoble.

With this model, when $\dot{z}$ is zero (steady-state speed), we come back to Coulomb based model (Figure 2.5) and so all the effects that one could expect when there is a certain relative speed between touching surfaces. The variable v is the velocity composed by the sum of inelastic and elastic displacement, as depicted in Figure 2.6 [5]. Here, we can say that

$$v = \dot{x} = \dot{z} + \dot{w}. \tag{2.7}$$

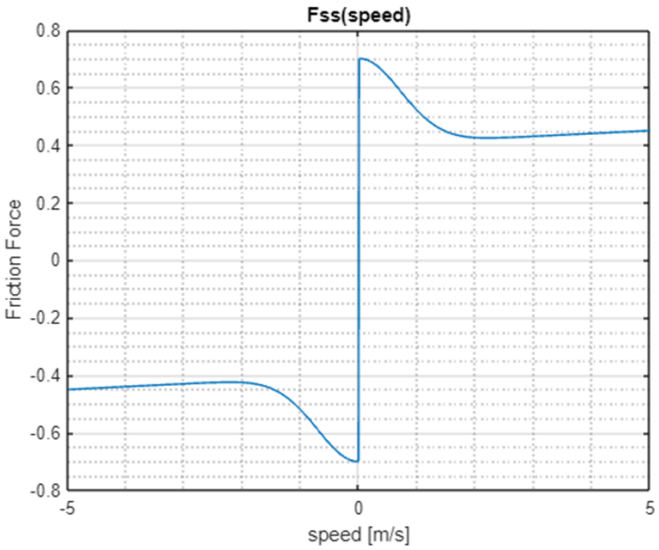

Figure 2.5: LuGre steady-state model.

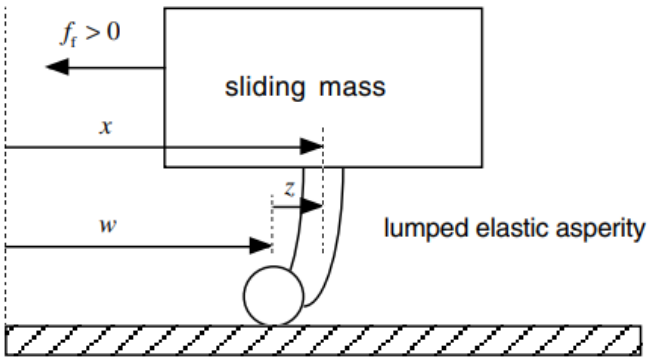

Figure 2.6: Displacement Decomposition [5].

Re-writing (2.7) and recalling (2.5), we can state that the terms in (2.7) correspond to

$$\begin{aligned} \dot{x} &= v, \\ \dot{w} &= \sigma_0 \cdot \frac{|v|}{g(v)} \cdot z. \end{aligned} \tag{2.8}$$

Therefore, the behaviour of the bristles should reflect the following conditions:

- If we are in sticking condition: $v = \dot{z}$, while $\dot{w} = 0$.
- If we are in sliding condition: $v = \dot{w}$, while $\dot{z} = 0$.

However, with the LuGre friction model, even in those situations where it indicates a sticking condition, which is characterized by having a force below the peak friction F_s, a small displacement w may still be present due to the absence of terms that force the velocity $\dot{w}$ to be zero.

2.2.2 Elasto-plastic model

The Elasto-Plastic model aims to be an improvement of the LuGre friction model where the additional parameter $\alpha(z, v)$ is introduced in the bristle displacement state equation[11][14], so that

$$\dot{z} = v - \sigma_0 \cdot \alpha(z, v) \cdot \frac{|v|}{g(v)} \cdot z. \tag{2.9}$$

This additional parameter is used to incorporate, in a better way, the pre-sliding displacement and the stiction. It is represented by the shape shown in Figure 2.7. It allows only elastic displacement of the bristles until the breakaway displacement z_{ba} is reached [11][14]. As reported in [14], it is analogous to the elastic deformation observed in a stress–strain curve. The breakaway displacement is linked to the point at which plastic deformation begins.

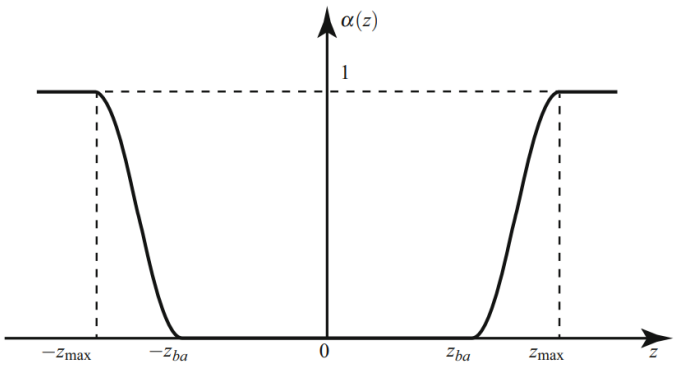

Figure 2.7: α-shape [11][14].

The difference and the improvement with respect to the LuGre model is that now, in sticking condition, $\dot{w}$ is forced to be zero and the only displacement allowed is the deformation of the bristles, but not their motion.

2.3 Experimental results with a simple case

With the aforementioned bristle surface formulations, it is now possible to replicate the stiction effect as well. To see how these models perform, let us consider the scenario of a wheel descending a hill with a brake pad subjected to braking pressure in

an attempt to stop the wheel motion (refer to Figure 2.8). The dynamic equilibrium equations of motion of this model are

$$m \cdot g \cdot \sin(\alpha) - F_t = m \cdot \ddot{x}, \tag{2.10a}$$

$$m \cdot g \cdot \cos(\alpha) - F_N = 0, \tag{2.10b}$$

$$\mu_p \cdot F_n \cdot R_m - F_t \cdot R_w = J_w \cdot \dot{\omega}, \tag{2.10c}$$

where the friction force comes into play in the braking pad as $F_b = \mu_p \cdot F_n$, when F_n is the applied braking force. Here the aim is to model F_b with the elasto-plastic theory. However, since the normal force F_n is not constant, it is more convenient to use the parameters of the elasto-plastic theory as the friction coefficient defining parameters. This ensures that the output of the model is just the coefficient μ_p, instead of the friction force. By doing so, we can vary the normal force F_n without considering this variation within the bristle state equation terms. The dynamic equations describing the friction behaviour become

$$\dot{z} = v - \sigma_0 \cdot \alpha(z, v) \cdot \frac{|v|}{g(v)} \cdot z, \tag{2.11a}$$

$$g(v) = \mu_d + (\mu_s - \mu_d) \cdot e^{-\left(\frac{v}{v_s}\right)^{\alpha}}, \tag{2.11b}$$

$$\mu_b = \sigma_0 \cdot z + \sigma_1 \cdot \dot{z} + \sigma_2 \cdot \dot{v}. \tag{2.11c}$$

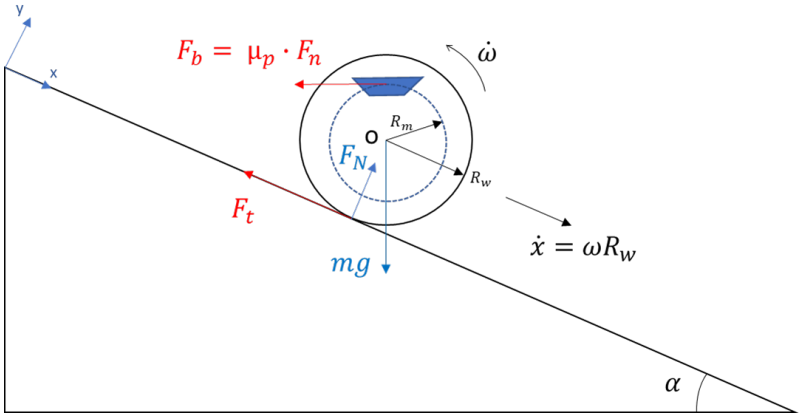

Figure 2.8: A wheel descending a hill equipped with a brake pad that is trying to stop the motion.

Let us analyze the results coming from simulating the wheel model represented by (2.10). Here the wheel initially has the speed $\dot{x} = 2$ [m/s] on a slope $\alpha = 15$ [°]. Figure 2.9 shows that the velocity of the wheel initially increases due to the action of the gravity force when the braking force is insufficient. However, the velocity eventually decreases until it reaches zero when the braking pressure further increases. With a simple Coulomb model, the friction forces would start to oscillate

as shown in Figure 1.2. With the bristle model mentioned in paragraph 2.2.1, it is possible to observe how the acceleration becomes zero as the motion stops. This demonstrates that bristle models can reproduce the stiction effect by generating a force that equals the sum of the external ones.

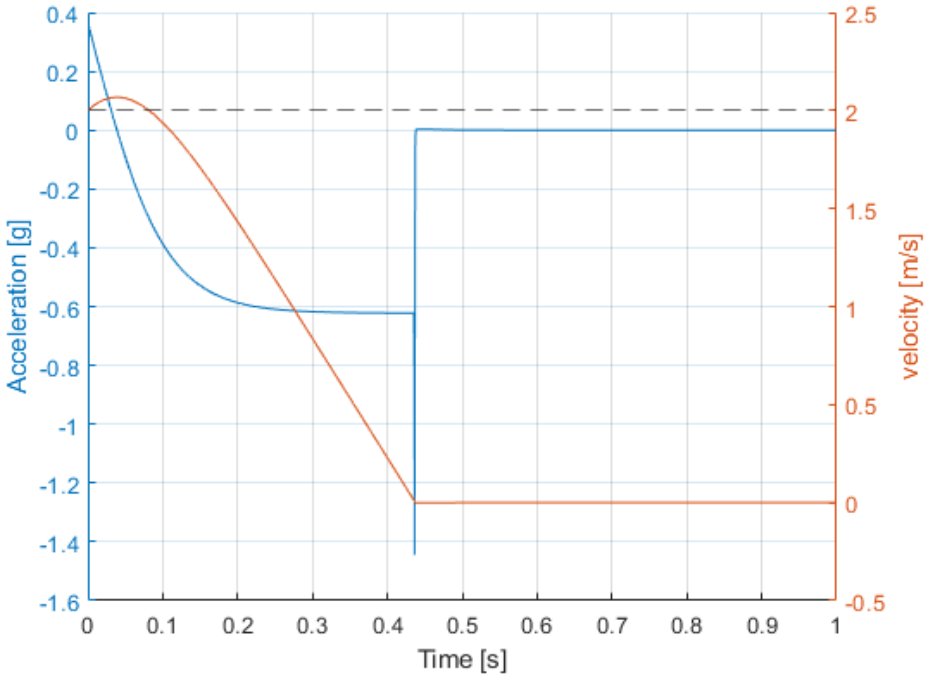

Figure 2.9: Wheel state behaviour with Elasto-Plastic friction.

Chapter 3

Tyre-ground force

Tyres are the only elements that allow the interaction between the vehicle and the ground. They allow the vehicle to be propelled by generating tangential forces with the ground. Therefore, having a proper model that accurately describes this exchange of forces is necessary to perform accurate simulations of real-world scenarios. The tangential forces are produced by the sliding motion between the tyres and the ground, which leads to the deformation of the rubber tyre tread and consequently, the generation of tangential stresses. To provide a better explanation of how this phenomenon occurs, a model known as the *brush model* is frequently used. This model, rather than being empirical, is a physically based model which accounts for friction level, load distribution and geometrical parameters of the tyre.

3.1 Brush model for longitudinal tyre force

The development of the model presented below holds under the following assumptions (see Figure 3.1):

- Steady-state conditions (the distributions of tyre tread shear deformation and shear stress are assumed constant over time, so no transition between operating conditions is considered).
- Parabolic and known pressure distribution over a constant and known contact patch length.
- Two different static and dynamic friction coefficients are considered.

Some nomenclature is also useful to understand the variables and the parameters involved:

ξ represents the tyre contact patch coordinate.
ξ_c represents the contact patch coordinate in which the bristles move from sticking to sliding conditions.
L is the total length of the contact patch.
H is the height of the rubber tread (represented by bristles).
W is the width of the contact patch.
γ is the angular deformation of the bristles.
τ represents the tangential stress created by the difference in speed between the belt and the ground (namely $v_r = \omega \cdot R - v_x$).

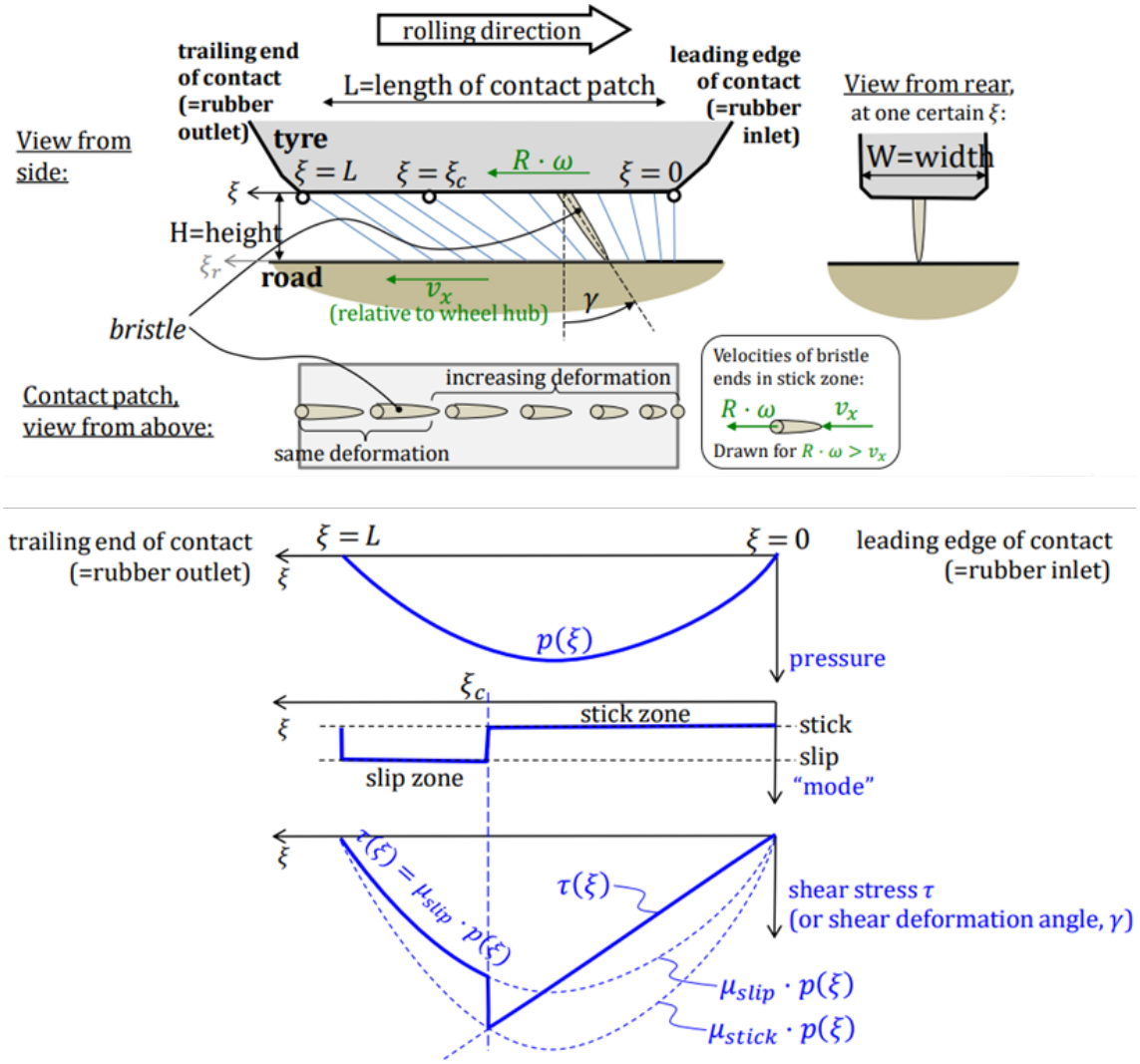

Figure 3.1: Brush Model under study with ξ representing the longitudinal coordinate from the contact patch inlet ($\xi = 0$) to the contact patch outlet ($\xi = 0$). Image taken from [7]

Figure 3.1 shows what happens within the contact patch of the tyre with the ground. Due to the friction and elastic characteristics of the tyre rubber, the rotation of the wheel induces a deformation of the bristles upon entering the contact patch due to the friction between the surface and the bristles themselves. When the friction remains below the peak static friction value, denoted by μ_s, the deformation of the bristles increases linearly with respect to the relative speed $v_r = \omega \cdot R - v_x$. However, once this peak value is exceeded, the bristles enter the sliding region where they slide over the ground. The friction is now governed by the dynamic friction coefficient, denoted by μ_d. At this point, as the friction decreases, τ also decreases, becoming proportional only to the normal load, which is in this case the pressure distribution.

It can be demonstrated (see [7, 12, 13]) that the tyre-ground force can be com-

puted using the slip-dependent formula of (3.1). For small slips close to the rolling case ($s_x \cong 0$), the force is directly proportional to the slip itself with a constant proportionality factor called *force-slip stiffness* C_x, as indicated in (3.1). However, as the slip increases, at a certain coordinate ξ_c in the contact patch the rubber tread (bristles) reaches the maximum deflection that the static friction coefficient can ensure and moves from the stick zone to the slip zone. This means that the force no longer increases linearly as some of the bristles start sliding, and this effect is captured by the second and third-order components in (3.1). At high levels of slip, when $\xi_c = 0$ all the bristles are slipping, the force is saturated and remains constant at the dynamic friction force $\mu_{slip} \cdot F_z$, similar to what is observed in classical Coulomb friction theory. This phenomenon occurs when the maximum amount of bristle *interlocking* (deformation) is overcome and none of the bristles is able to generate additional friction force.

$$F_x = \begin{cases} \mu_{slip} \cdot F_z \cdot sign(s_x), & \text{if } \omega \cdot v_x < 0 \text{ or } \xi_c < 0 \\ \left(C_x \cdot |s_x| - \left(2 - \frac{\mu_d}{\mu_s}\right) \cdot \frac{(C_x \cdot |s_x|)^2}{3 \cdot \mu_s \cdot F_z} + \right. & \\ \qquad \left. \left(3 - 2 \cdot \frac{\mu_d}{\mu_s}\right) \cdot \frac{(C_x \cdot |s_x|)^3}{27 \cdot (\mu_s \cdot F_z)^2}\right) \cdot \text{sign}(s_x), & \text{else} \end{cases} \tag{3.1}$$

$$\text{With} \quad C_x = \frac{G \cdot W \cdot L^2}{2 \cdot H} \quad \text{and} \quad s_x = \frac{\omega \cdot R - v_x}{|\omega \cdot R|}$$

What comes out from (3.1) can be seen in Figure 3.2. This is a simplified physical model of a real tyre which does not consider, for instance, the tyre carcass compliance, as well as possible tyre tread and carcass damping and viscous effects. However, it is useful to understand the relationship with the slip variable, and it also provides a physical explanation of why and how the slip is generated.

3.2 Empirical model for longitudinal tyre force

In cases where a specific tyre characteristic is well-known and experimental data are available, semi-empirical models can be used to determine the tyre-ground force as a function of the slip s_x. These models make use of empirical mathematical functions to fit experimental data. One of the most renowned curve-fit tyre models is the so-called *Magic Formula*, which was proposed by Professor Hans Pacejka [13]. The curve-fit *Magic Formula* can be expressed as

$$y = D \cdot (C \cdot \arctan(B \cdot x - E \cdot (B \cdot x - \arctan(B \cdot x)))). \tag{3.2}$$

Here, y represents the quantity of interest, such as longitudinal force F_x, while x represents the quantity on which y depends (the slip s_x for longitudinal forces). Other parameters are introduced to fit the experimental data. The so-called slip-stiffness C_x, which represents the slope $\left.\frac{dy}{dx}\right|_{x=0}$ of the curve, is modelled using the

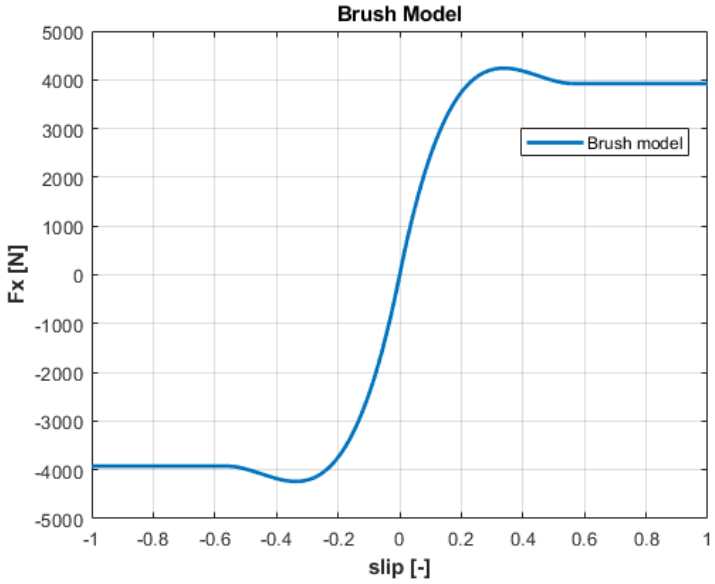

Figure 3.2: Force-slip characteristic of the brush model under study with $C_x = 31392$ [N/-], $\mu_s = 1.5$, $\mu_d = 1$, $F_z = 400 \cdot g$ [N]

parameter $\arctan(B \cdot C \cdot D)$, as illustrated in Figure 3.3. To represent the saturation effect, the *Magic Formula* employs the arctangent function, where the peak force is determined by the parameter D. Additional parameters are used to shape the curve to match the experimental data. The coefficients S_H and S_V, visible in Figure 3.3, allow for a new set of coordinates Y(X) to be introduced (see [13]), so that

$$Y = D \cdot (C \cdot \arctan(B \cdot X - E \cdot (B \cdot X - \arctan(B \cdot X)))), \tag{3.3}$$

where $Y = y + S_V$ and $X = x + S_H$. This is done to account for any uncertainty in the experimental data measurements and to consider forces that arise for particular tyre plies configurations as well as the rolling resistance effect.

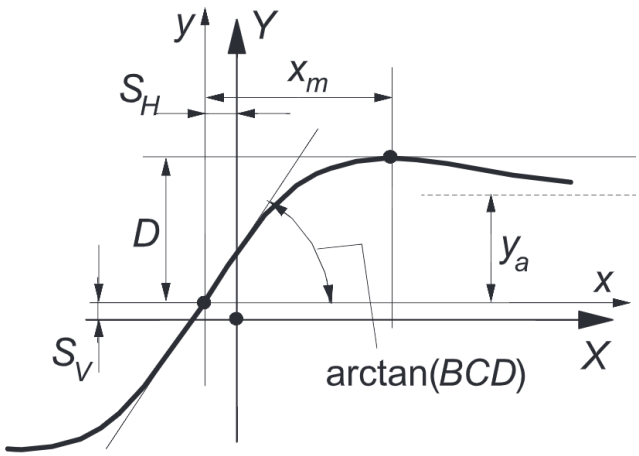

Figure 3.3: Magic Formula - influence of the different parameters (picture from Pacejka book, [13]).

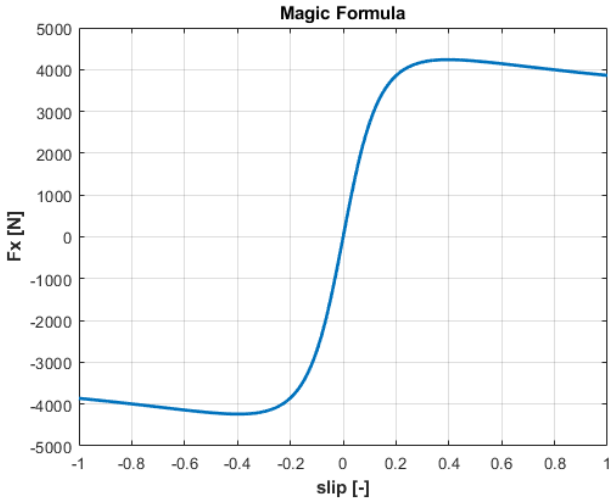

Figure 3.4: Magic Formula force-slip characteristic

Having listed the two most common approaches to the problem of tyre-ground forces generation, it is important to notice the issue mentioned in section 1.2. Having that the tyre slip ratio is defined as

$$s = \frac{\omega \cdot R - V}{|\omega \cdot R|}, \tag{3.4}$$

when $\omega \cdot R$ approaches zero numerical problems occur as the slip becomes very large or undefined for $\omega \cdot R = 0$. Therefore, the goal of the next chapter will be to find out a formulation which can give a longitudinal force proportional to something different from the slip, to have a model which can work well at any speed.

Chapter 4

Modelling and simulation

In this chapter, different techniques and friction formulations are evaluated using a basic dynamic model (see Figure 4.1). Here simulations of both tyre slip and friction between brake pads and disc are performed. Initially, simulations of those two effects are conducted separately to examine the effects of brake friction with a non-slipping wheel, and the impact of tyre slip in the absence of brake friction. Later, both factors will be taken into account to observe their interaction.

4.1 Brake models

Recalling the dynamic system shown in Figure 4.1, the aim here is to find and use a model which is capable of describing how the friction force between the brake pads and disc behaves.

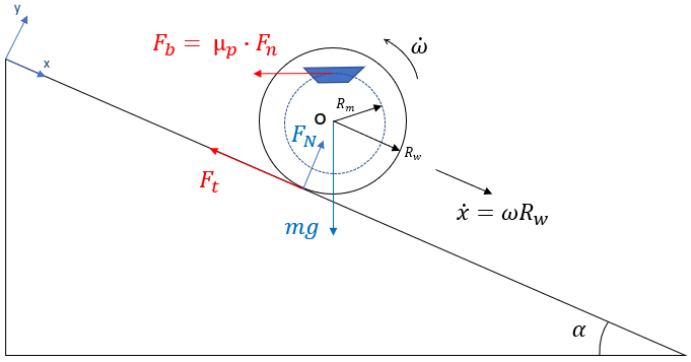

Figure 4.1: A wheel equipped with a disc brake that is braking it to stop the motion.

To do so, it is first useful to recall the dynamic equations describing the motion of the wheel to better see where the problems arise. First, considering the brake actuated by oil pressure, we can write the normal force acting on the pads as

$$F_n = \pi \cdot R_p^2 \cdot p, \tag{4.1}$$

where p is the brake line pressure in [bar] and R_p the brake pad cylinder radius in [m]. Knowing that the relationship between the normal force and the brake force is determined by the friction between the pads and the disc, the braking force and torque can be expressed as

$$F_b = \mu(\omega) \cdot F_n = \mu(\omega) \cdot \pi \cdot R_p^2 \cdot p \cdot \text{sign}(\omega), \tag{4.2a}$$

and

$$T_b = N \cdot R_m \cdot \mu(\omega) \cdot \pi \cdot R_p^2 \cdot p \cdot \text{sign}(\omega), \tag{4.2b}$$

where

N is the number of brake pads.
R_m is the mean pads radius [m].
μ is the friction coefficient [-].

Knowing how this force behaves, the dynamic equilibrium of the wheel in Figure 4.1 is given by

$$m \cdot g \cdot \sin(\alpha) - F_t = m \cdot \ddot{x}, \tag{4.3a}$$

$$m \cdot g \cdot \cos(\alpha) - F_N = 0, \tag{4.3b}$$

$$N \cdot R_m \cdot \mu(\omega) \cdot \pi \cdot R_p^2 \cdot p \cdot \text{sign}(\omega) - F_t \cdot R_w = J_w \cdot \dot{\omega}, \tag{4.3c}$$

where

J_w is the wheel inertia [kg·m^2].
R_w is the wheel radius [m].
$\ddot{x}$ is the wheel longitudinal acceleration [m/s^2]
$\dot{\omega}$ is the wheel rotational acceleration [rad/s^2].

At this point, the goal becomes to be able to properly formulate $\mu(\omega)$. Recalling the Benson friction model presented in 2.2, we have that the friction coefficient can be described with the exponential function

$$\mu(\omega) = \begin{cases} \mu_s, & \omega = 0 \\ \mu_d + (\mu_s - \mu_d) \cdot e^{-(\frac{\omega \cdot R}{v_s})^{\alpha}}, & \omega \neq 0 \end{cases} \tag{4.4}$$

It has been already pointed out how this kind of model is not able to describe the stiction phenomena, but it will be used to compare the results with more advanced friction models (see section 2.2). Using such a simple model to describe the friction and taking the following initial conditions for the system:

$$\dot{x}_0 = 2 \text{ [m/s]},$$

$$\dot{\omega}_0 = \frac{\dot{x}_0}{R_w} \text{ [rad/s]}$$

and a linearly increasing brake line pressure with time t:

$$p = \max(p_{max} \cdot t,\ \ p_{max}), \qquad \text{subjected to } \ p_{max} = 40 \cdot 10^5 \ \text{[Pa]}, \tag{4.5}$$

the wheel shows the behavior reported in Figure 4.2. When the wheel comes to a complete stop, the friction force (that is proportional to the acceleration) starts to oscillate between its peak values (the blue area are oscillations at high frequency) for the reasons explained in section 1.1. Despite the mean value remaining equivalent to the sum of external forces, or in the case of acceleration, equal to zero, the stiction phase can not be captured. The behaviour of the friction force (and consequently of the acceleration, which is what we want to capture and analyze) shows a non-physical oscillating trend as the speed approaches zero.

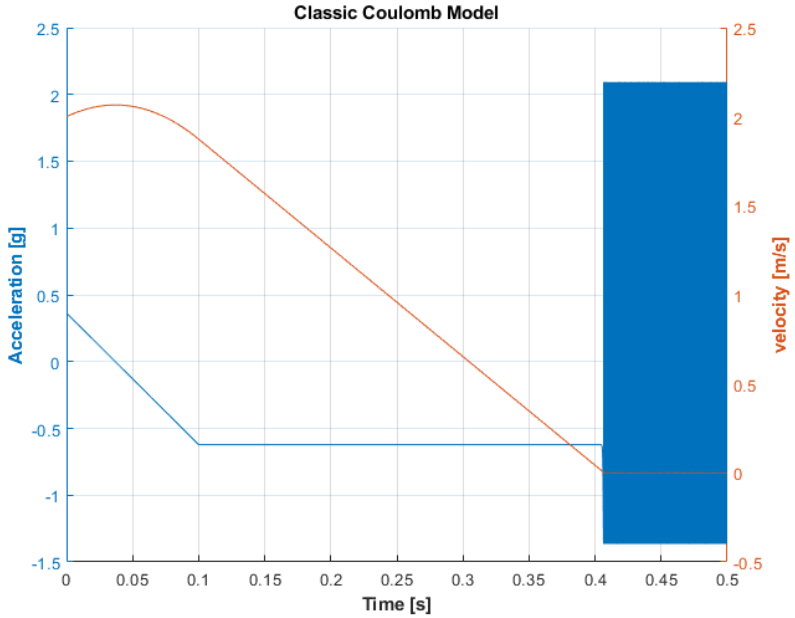

Figure 4.2: Behavior of the wheel acceleration and speed while being decelerated by the brake modelled with the classic Coulomb theory implemented with Matlab sign-function.

4.1.1 State-based approach

One relatively simple way to deal with stiction and have a simulation tool capable of giving the proper static force for zero speed is to implement a state machine. The principle of working is to use two different states when the relative speed ω of the two sliding surfaces is different or equal to zero. In particular, when $\omega \neq 0$ the state machine will output the friction force coming from (2.2). When, instead, $\omega = 0$ the state will change and the machine will output the force resulting from the steady-state equilibrium condition which can be computed by setting the accelerations in (4.3) equal to zero (see (4.6)).

$$m \cdot g \cdot \sin(\alpha) - F_t = 0, \tag{4.6a}$$

Table 4.1: Wheel and pads parameters used to simulate model 4.3

Parameter of the model			
m	[kg]	Wheel Mass	68.75
J_w	[kg·m^2]	Wheel Inertia	0.23
R_w	[m]	Wheel Radius	0.24
μ_s	[-]	Peak friction coefficient	0.70
μ_d	[-]	Dynamic friction coefficient	0.40
N	[-]	Number of pads	2
A_p	[m^2]	Pad cylinder area	$4.50 \cdot 10^{-4}$
v_s	[m/s]	Stribeck velocity	0.02

$$m \cdot g \cdot \cos(\alpha) - F_N = 0, \tag{4.6b}$$

$$N \cdot R_m \cdot F_b - F_t \cdot R_w = 0. \tag{4.6c}$$

By substituting (4.6c) in (4.6a) we obtain

$$F_{b,ss} = \frac{m \cdot g \cdot \sin(\alpha) \cdot R_w}{N \cdot R_m}. \tag{4.7}$$

At this point, an example of the implementation of this state machine on Simulink© can be seen in Figure 4.3.

Using this approach the results for the dynamic system described by (4.30) are shown in Figure 4.4 and Figure 4.5. It can be noticed that now, as the wheel comes to a stop, the acceleration and the resulting friction force exhibit behaviour that accurately reflects real-world physics. Initially, as the speed approaches zero, the Stribeck effect causes the friction force to increase up to its peak value, resulting in a negative acceleration peak at approximately 0.4 seconds. Following this, the acceleration abruptly drops to zero while the friction force becomes equal to $F_{b,ss}$, as illustrated in Figure 4.5. The stiction phenomenon is now captured.

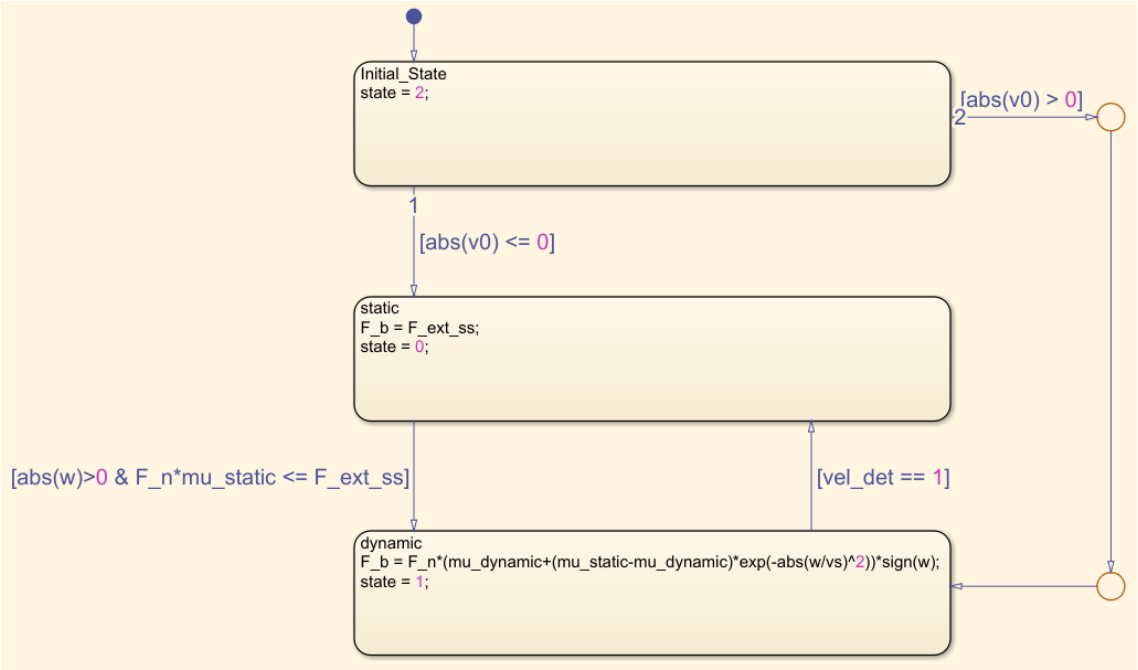

Figure 4.3: State transition chart on Simulink©, the state transitions are regulated by the speed (*vel_det* is the zero speed crossing detector). Additional conditions on forces are inserted to increase robustness and avoid numerical error, i.e., very small speed changes around zero due to the machine precision.

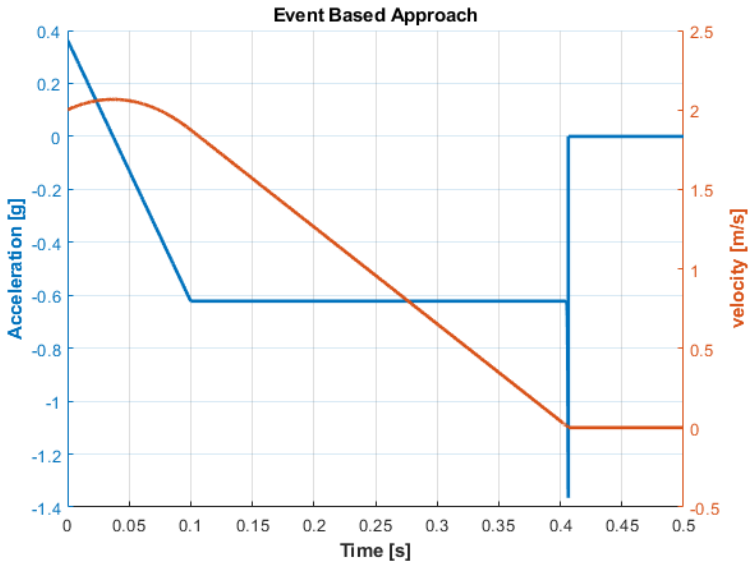

Figure 4.4: Behavior of the wheel acceleration and speed with the friction regulated by a state-transition table.

4.1.2 The bristle models approach

Recalling what was said in section 2.2.2, using the bristle theory it is possible to implement a friction model which can be described by the deformation of bristles. In particular, they represent the asperity of the surfaces in contact and their deflection

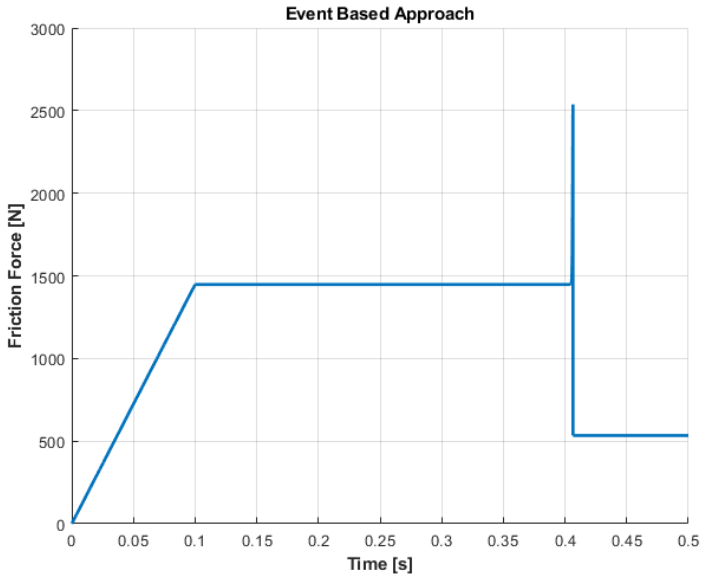

Figure 4.5: Behavior of the brake friction force.

is proportional to the friction. Implementing this kind of model with the parameter of Table 4.2 leads to the results shown in Figure 4.6.

Table 4.2: Parameters of the elasto-plastic model used simulate model 4.3

Parameter of the model			
σ_0	[1/m]	Bristle stiffness	$1.48{\cdot}10^{3}$
σ_1	[s/m]	Bristle micro-damping	38.50
σ_2	[s/m]	Sliding viscosity factor	0
v_s	[rad/s]	Stribeck velocity	$2.13{\cdot}10^{-2}$
z_{ba}	[m]	Brake-away bristle displacement	$0.10{\cdot}10^{-3}$
z_{max}	[m]	Maximum bristle elastic displacement	$6.60{\cdot}10^{3}$

As for the state-based model, when the wheel speed approaches zero, the Stribeck effect causes the friction force to increase up to its peak value. During this process, the bristles experience a deflection in the opposite direction to the speed. However, as the speed continues to decrease and approaches zero, the Stribeck effect causes this deformation to increase to its maximum value. At this stage, according to (2.7), the velocity $\dot{w}$ becomes zero, and the wheel comes to a stop. The bristles then return to their steady-state position, where they exert a force to keep the wheel still, as shown in Figure 4.7.

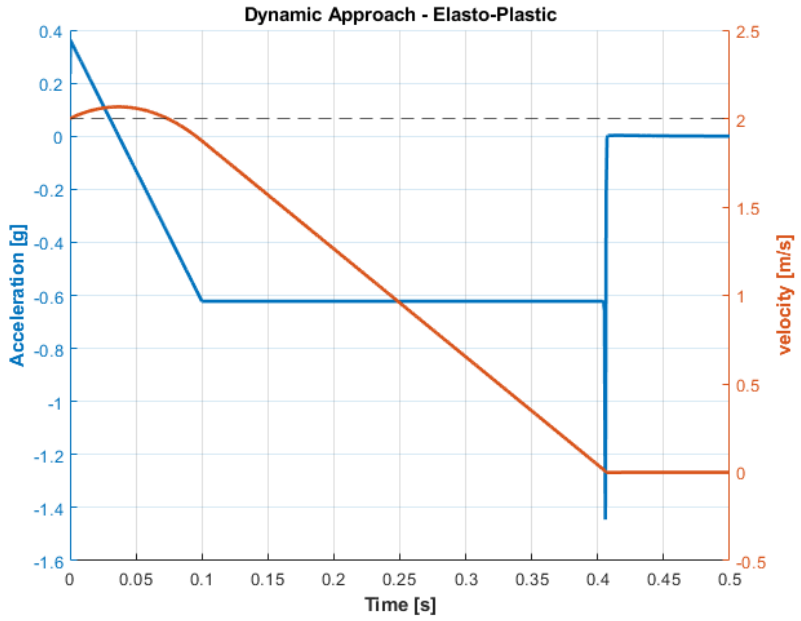

Figure 4.6: Behavior of the wheel acceleration and speed with the Elasto-Plastic friction model (2.11).

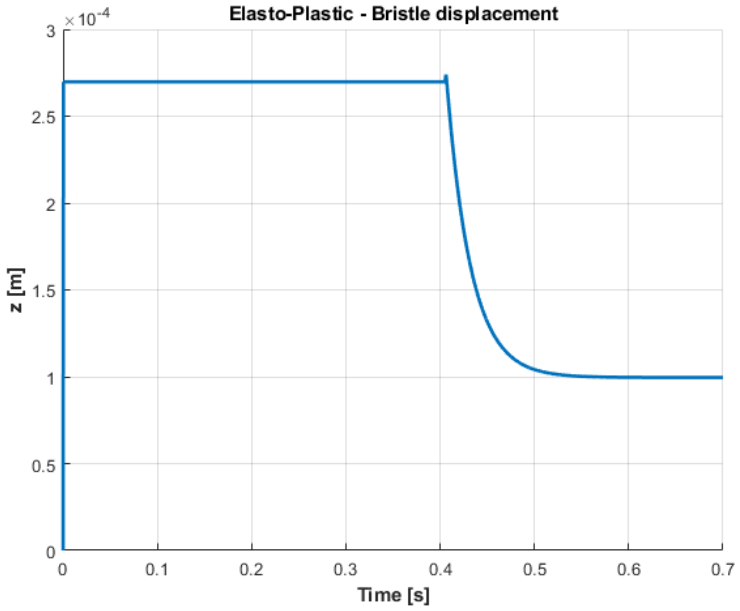

Figure 4.7: Behavior of the bristles with the Elasto-Plastic friction model (2.11).

4.1.3 Considerations

Three different kinds of friction models have been considered in this stage. The results show how, when the speed is zero, the classic frictions theory requires more advanced numerical techniques to capture real physics phenomena.

4.2 Tyre-ground force - LuGre tyre model

Having analyzed how to model the friction with brakes, it is now time to deal with tyre-ground force generation. As introduced in section 1.2, when the rotational speed of the wheel is zero, the slip (1.6) is not mathematically defined anymore. During simulations, this translates to problems in understanding how exactly the tyre-ground force behaves at low speeds. The goal of this section is then to define a new tyre model which can handle this singularity and which does not make use of slip to work. To this purpose, the LuGre-brush formulation will be presented in the following sections as it provides a theoretical framework to explore tyre-ground interaction without separating the contact patch into an adhesion region and a sliding region as it happens for the brush-model [4, 9, 16].

4.2.1 LuGre tyre model derivation

As in the case of brakes, we can consider the tyre tread to interact with the ground through bristles which deflect. With reference to Figure 4.8 we can introduce some assumptions to study the model behaviour:

- Bristles are considered hinged at the belt base (see Figure 4.9).
- Bristles are considered massless.
- Bristles do not interact with each other (they are not connected).
- The angular deformation γ is considered small.
- Known force distribution over a constant and known contact patch length L.

Some nomenclature is also useful to proceed with the treaty:

ξ represents the tyre contact patch coordinate.
L is the total length of the contact patch.
H is the height of the bristles.
γ is the angular deformation of the bristles.
z is the projection of the bristles to the ground obtained as $\gamma \cdot H$ for small angles.
v_r represents the relative velocity between the wheel and the ground.

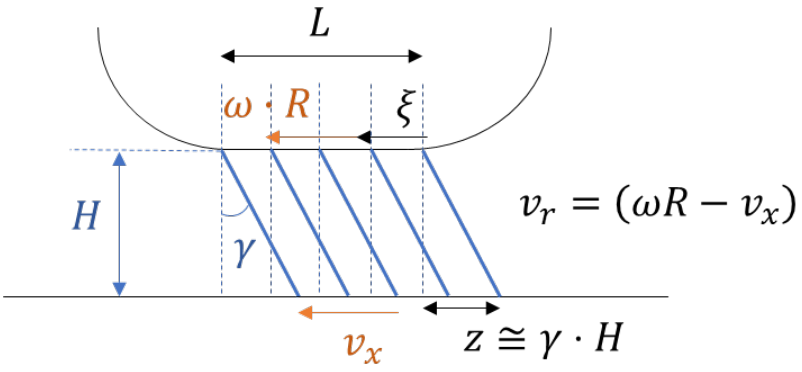

Figure 4.8: Behavior of the bristles with the Elasto-Plastic friction model.

To start, with reference to Figure 4.8, we can define as the state variable of the model the horizontal bristle deflection $z(\xi, t)$ at the base point position $0 \leq \xi \leq L$ and at certain time t [4]. With reference to the Eulerian specification of the motion field, if we look at a fixed control volume of the contact patch, the total derivative of the bristle deflection can be written as

$$\frac{dz(\xi,t)}{dt} = \frac{\partial z(\xi,t)}{\partial t} + \frac{\partial z(\xi,t)}{\partial \xi} \cdot \frac{\partial \xi}{\partial t}, \tag{4.8}$$

with the term $\frac{\partial \xi}{\partial t}$ that, as demonstrated in Appendix A, can be set equal to

$$\frac{\partial \xi}{\partial t} = |\omega \cdot R|. \tag{4.9}$$

At this point, some considerations on the bristles have to be made to describe their motion. The concept of friction force, as shown in [6], arises from the fact that the bristles can be viewed as being hinged to the tyre carcass and their motion is linked to a sort of spring stiffness (which can be explained with simple Hooks law on a sheared short rubber beam) denoted with σ_0 and a damper (which can be explained with viscous properties of the sheared short rubber beam) denoted with σ_1 (see Figure 4.9).

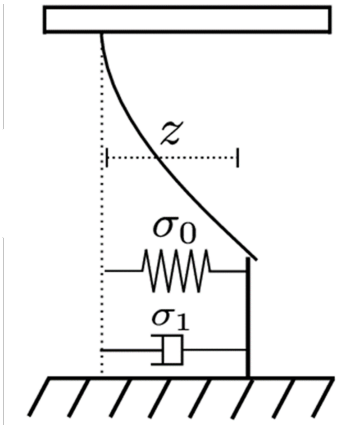

Figure 4.9: The bristle are hinged to the wheel carcass and their motion linked by the spring deformation [6].

Considering the bristle deflection derivative equal to

$$\dot{\gamma} = \frac{v_r}{H} \tag{4.10a}$$

and

$$z(\xi, t) = \gamma \cdot H, \tag{4.10b}$$

we have that

$$\frac{dz(\xi,t)}{dt} = v_r. \tag{4.11}$$

At the same time, due to limited tyre/road friction potential, the deflection of the bristles needs to be saturated to the maximum grip potential [4]. This saturation can be introduced considering the additional term

$$\frac{\sigma_0 \cdot |v_r|}{g(v_r)} \cdot z(\xi, t), \tag{4.12}$$

with

$$g(v_r) = \mu_d + (\mu_s - \mu_d) \cdot e^{-\left(\frac{|v_r|}{v_s}\right)^a}, \tag{4.13}$$

which represent the bristles' friction behaviour for different relative speeds v_r. Adding the saturation term of (4.12) in (4.11) we can rewrite the total horizontal bristle deflection derivative as

$$\frac{dz(\xi, t)}{dt} = v_r - \frac{\sigma_0 \cdot |v_r|}{g(v_r)} \cdot z(\xi, t). \tag{4.14}$$

In this way, when the deflection limit $\frac{g(v_r)}{\sigma_0}$ is reached, we have

$$z(\xi, t) = \frac{g(v_r)}{\sigma_0} \tag{4.15}$$

and so

$$\frac{dz(\xi, t)}{dt} = v_r - \frac{\sigma_0 \cdot |v_r|}{g(v_r)} \cdot z(\xi, t) = v_r - |v_r| \cdot \text{sign}(z(\xi, t)) = 0. \tag{4.16}$$

This means the bristles are not deforming anymore and they are sliding within the contact patch. At this point, re-arranging (4.8), we obtain

$$\frac{\partial z(\xi, t)}{\partial t} = v_r - \frac{\sigma_0 \cdot |v_r|}{g(v_r)} \cdot z(\xi, t) - |\omega \cdot R| \cdot \frac{\partial z(\xi, t)}{\partial \xi}. \tag{4.17}$$

The state equation (4.17) represents the bristle deformation behaviour over the contact patch. Thus, knowing the deformation, the friction between each bristle and the ground can be written as

$$\mu(t, \xi) = \sigma_0 \cdot z(t, \xi) + \sigma_1 \cdot \frac{\partial z(\xi, t)}{\partial t} + \sigma_2 \cdot v_r, \tag{4.18}$$

with σ_2 that represents the tyre viscous effect on slippery surfaces. Note that, as pointed out in [4], the term σ_1 just multiplies the partial derivative of the horizontal bristle deflection over time because it does not need to dampen the tyre force oscillations over the space. That would be non-physical.

At this point, having the friction and knowing the vertical force distribution over the contact patch, the tyre-ground force can be computed by integrating the bristle horizontal force

$$dF_x(t, \xi) = \mu(t, \xi) \cdot p(\xi) \cdot d\xi \tag{4.19}$$

over the contact length [4, 16, 3, 17], so that

$$F_x(t) = \int_0^L dF_x(t,\xi) = \int_0^L \mu(t,\xi) \cdot p(\xi) \cdot d\xi. \tag{4.20}$$

4.2.2 LuGre discrete model

The dynamic tyre model described above is evaluated through computer simulation to determine its response [4]. To this purpose, the mentioned continuous model of (4.17) is discretized in N bristles [4], so that the partial derivative over the contact patch coordinate $\dfrac{\partial z(\xi,t)}{\partial \xi}$ can be written as

$$\frac{\Delta z(N,t)}{\Delta \xi} = \frac{z_{i+1}(t) - z_i(t)}{\Delta \xi} = \frac{z_{i+1}(t) - z_i(t)}{L} \cdot (N-1), \tag{4.21}$$

with z_i representing the i^{th} bristle deflection and the term $\Delta\xi = \dfrac{L}{N-1}$ the distance between each bristle.

In this way, (4.17) becomes a set of N ordinary differential equations (ODEs), where

$$\dot{z}_i(t) = v_r - \frac{\sigma_0 \cdot |v_r|}{g(v_r)} \cdot z_i(t) - |\omega \cdot R| \cdot \frac{z_{i+1}(t) - z_i(t)}{L} \cdot (N-1). \tag{4.22}$$

In turn, (4.18) becomes

$$\mu_i(t) = \sigma_0 \cdot z_i(t) + \sigma_1 \cdot \dot{z}_i(t) + \sigma_2 \cdot v_r \tag{4.23}$$

and (4.20):

$$F_x(t) = \sum_{i=1}^{N} \mu_i(t) \cdot p_i \cdot \Delta\xi. \tag{4.24}$$

4.2.3 LuGre discrete model results

Some considerations can be made by simulating the model of (4.24) for a range of relative speeds and looking at what happens inside the contact patch and to the resultant friction force. The parameters shown in Table 4.3 have been used to analyze the model.

Table 4.3: LuGre parameters used to simulate the discrete tyre model of (4.24)

Parameters of the model								
N	L [m]	a [-]	σ_0 [1/m]	σ_1 [s/m]	σ_2 [s/m]	v_s [rad/s]	μ_s [-]	μ_d [-]
200	0.3	0.8	195	2	0	4	1.87	0.82

Figure 4.10 shows the bristle force and horizontal displacement behaviour while moving from $\xi = 0$ to the trailing edge of the contact patch $\xi = L$. The model

makes use of a parabolic normal load distribution which trend can be obtained by solving the following system of equations:

$$\begin{cases} F_z = \int_0^L p(\xi)d\xi, \quad \text{subjected to } p(0) = p(L) = 0, \\ p(\xi) = a \cdot x^2 + b \cdot x + c, \end{cases} \tag{4.25}$$

which leads to

$$p(\xi) = \frac{6 \cdot F_z}{L^2} \cdot \xi \cdot \left(1 - \frac{\xi}{L}\right), \tag{4.26}$$

that for a discretized problem turns out to

$$p(i) = \frac{6 \cdot F_z}{L} \cdot \frac{i-1}{N-1} \cdot \left(1 - \frac{i-1}{N-1}\right). \tag{4.27}$$

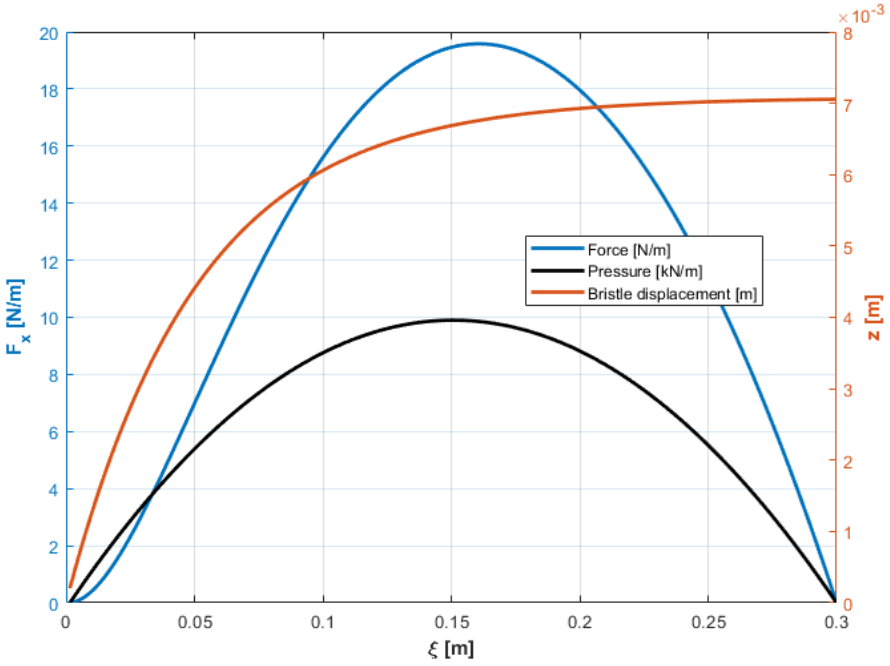

Figure 4.10: Bristle friction force and displacement at the relative velocity of v_r 2.33 [m/s].

It can be noticed how the bristles horizontal displacement z does not completely reflect the reality. In fact, as one would expect, it increases almost linearly at the very beginning in the contact patch, but then the saturation term of (4.12) introduces an exponential behaviour along ξ, with $z_{max} = \dfrac{g(v_r)}{\sigma_0}$ reached at the end of the contact patch. Making some calculation for $v_r = 2.33$ [m/s] we have that

$$g(v_r) = \mu_d + (\mu_s - \mu_d) \cdot e^{-\left(\frac{|v_r|}{v_s}\right)^a} = 1.378 \ ,$$

which gives

$$z_{max} = \frac{g(v_r)}{\sigma_0} = 0.0071 \ \text{[m]}.$$

Knowledge of physical tyres (like the classic brush model theory) show how the deflection of the bristles should initially increase, but after reaching a peak value around the peak vertical load, it should then decrease to zero at the trailing edge of the contact patch (see Figure 4.11) [9]. There, indeed, no loads or forces are acting on the bristles.

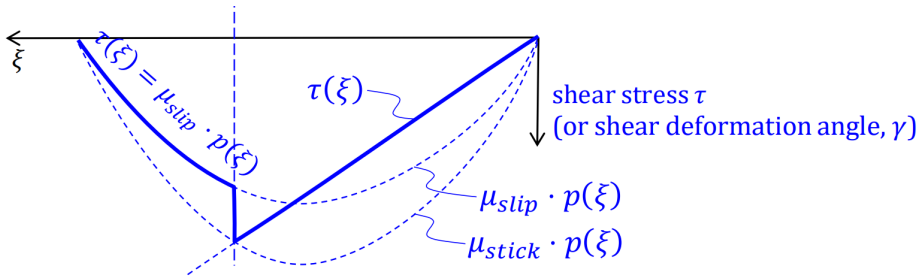

Figure 4.11: Brush model with parabolic pressure distribution [7]. Initially, the deformation (proportional to the shear stress τ) shows a linear increase up to the point of static friction peak. However, after reaching this peak, a drop in deformation occurs due to friction saturation.

However, this model does not account for the vertical load in the bristle deflection state equation. Nevertheless, the blue curve in Figure 4.10, which represents the longitudinal force distribution, approximates the real-world behaviour quite well as the force initially increases at a rate dependent on the vertical load, but eventually returns to zero at the trailing edge, denoted as $\xi = L$.

4.2.4 LuGre tyre model - speed dependency

Recalling (4.17) it can be seen how this model is a function of two variables, i.e. the relative speed between the tyre and the ground v_r and the rotational speed of the wheel ω. To understand how this influence this model it is useful to recall the concept of slip in order to have a parameter of comparison with a well-known model like the Pacejka one (which instead depends only on the slip (1.6)). To this purpose, simulations are carried out with different values of relative speeds and rotational velocities and the resultant forces are then plotted as a function of the slip (see Figure 4.12)

$$s = \frac{\omega \cdot R - v_x}{|\omega \cdot R|}.$$

In particular, the relative velocity is made to vary for a fixed rotational speed and the process is repeated for different values of the latter to capture the force behaviour at different slips and different relative velocities. Additionally, a comparison with the empirical Pacejka model will be presented to highlight the differences between the two models. The simulation parameters for the LuGre tyre model are taken

from Table 4.3, while those for the Pacejka model are from Table 4.4. Examining Figure 4.12, it is apparent that the force exhibits a speed dependency in the saturation region, unlike the Pacejka tyre model (indicated by the dashed blue line). Specifically, as the relative velocity increases, the force decreases. This phenomenon can be attributed to the terms (4.12) and (4.13). As the relative speed increases, the friction term (4.13) decreases, which leads to an increase in the saturation term (4.12). This, in turn, causes a decrease in the maximum bristle deflection. This also explains why the force reduction is lessened beyond a certain speed, as (4.13) saturates at the dynamic friction coefficient value. A minor additional change in force can be due to the viscous term $\sigma_2 \cdot v_r$ of (4.18) (in this case it is 0).

Table 4.4: Pacejka model parameters

Parameters of the model			
B [N/-]	C [-]	D [N]	E [-]
0.18	1.51	2050	0.432

The accuracy of the LuGre tyre model results has yet to be confirmed by experimental evidence. However, it appears to be plausible to incorporate this speed dependency into an appropriate tyre model. Let us consider the specific scenario of locking the wheel while braking. Under such conditions, the wheel essentially becomes a moving mass that is decelerated by friction with the ground. It is evident that as the friction acts on the wheel and it decelerates (resulting in a decrease in relative speed), we move from the dynamic friction zone to the static one. As a result, the friction force increases (as depicted in Figure 2.2), which agrees with the behaviour of the LuGre tyre model.

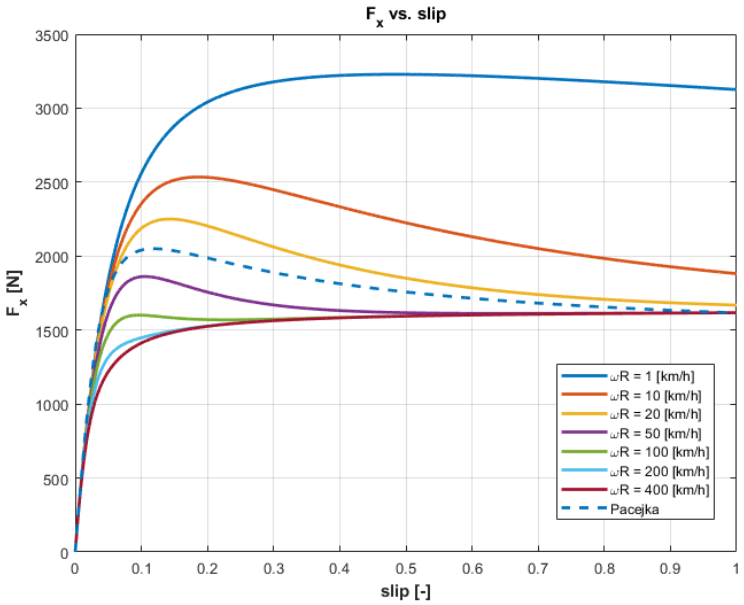

Figure 4.12: Force behaviour for the LuGre tyre model at different angular speeds.

4.2.5 |s| higher than 1

Up until now, we have only compared the Pacejka tyre model with the LuGre tyre model within the slip range of 0 to 1. However, let us now consider a scenario in which the wheel is rotating in the opposite direction relative to the longitudinal speed or the term $\omega \cdot R$ is very low. If this is the case, the slip will eventually exceed values greater than 1. From Figure 4.13 it can be seen how, without properly tuning the two models to match, the saturation region of the force is reached for different slip values and the saturated force shows some differences between the two models. As shown in Figure 4.14, analyzing the two opposite scenarios where either $v_x = 0$ or $\omega \cdot R = 0$, it becomes evident that there is a variation in the force when $\omega \cdot R = 0$ and v_x increases due to the fact that the slip is ideally infinite. On the contrary, when $v_x = 0$ and $\omega \cdot R$ vary (slip $= 1$), the two models achieve the same level of force.

However, the two models should behave in the same manner, at least in those conditions in which the slippage is very high. This is due to the fact that in such instances, all bristles are slipping in relation to the ground, causing the term (4.12) to have an identical effect on each bristle, as they have all reached the saturation limit of (4.13). As a result, the partial derivative

$$\frac{\partial z(\xi, t)}{\partial \xi}$$

will be zero, and the only factor contributing to a displacement (and consequently a force) will be the relative velocity v_r. Thus, the LuGre model parameter can be appropriately adjusted to make the model suitable for the aforementioned conditions. The parameters result from the tuning are shown in Table 4.5 and the force behaviour results are visible in Figure 4.15 and Figure 4.16.

Table 4.5: LuGre tyre model parameters after tuning

Parameters of the model								
N	L [m]	a [-]	σ_0 [1/m]	σ_1 [s/m]	σ_2 [s/m]	v_s [rad/s]	μ_s [-]	μ_d [-]
100	0.1	0.42	650	2	0	3.2	1.95	0.73

A useful measure of how and where the LuGre model differs from the Pacejka model can be appreciated in Figure 4.17, where the root mean square error(RMSE) between the two is plotted as a function of v_r and $\omega \cdot R$. The areas where the LuGre model diverges from the Pacejka model are primarily located in regions where we seek to eliminate the singularity of a slip-based model, particularly for very small $\omega \cdot R$ values. Moreover, the dependency of the LuGre tyre model on the speed can be appreciated in those regions (in light blue) where the slip value and the relative speed $\omega \cdot R - v_x$ are small (see Figure 4.18). Thus, where the contribution of (4.13) leads to a difference between the two models.

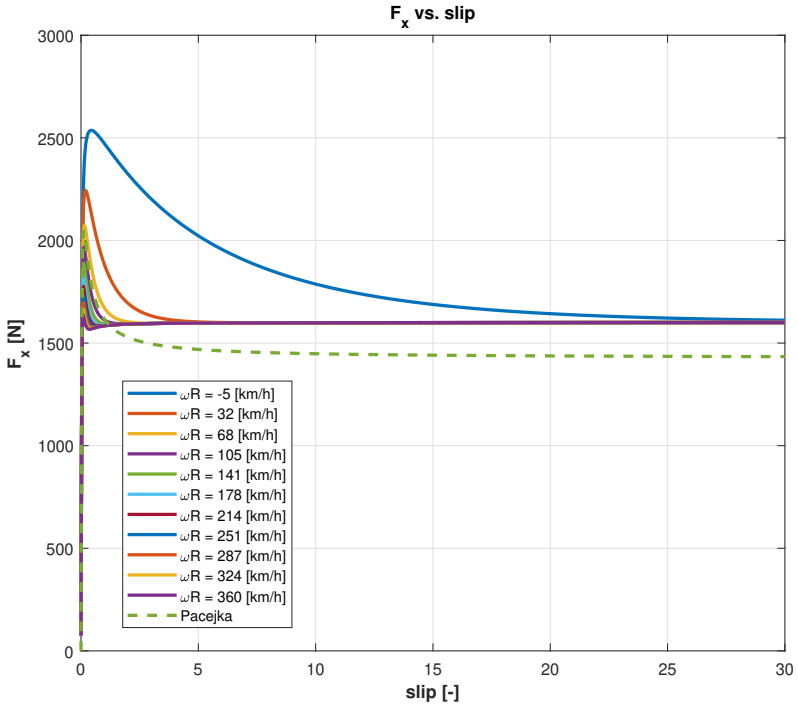

Figure 4.13: Force behaviour for slip values higher than 1.

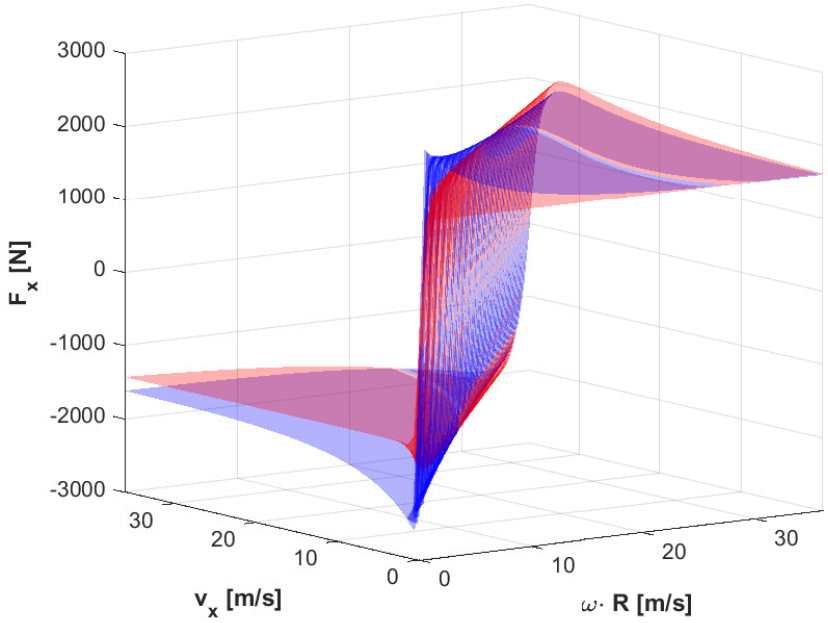

Figure 4.14: Force behaviour plotted as a function of the longitudinal speed v_x and the rotational velocity $\omega \cdot R$, in red the Pacejka force surface, in blue the LuGre model tyre force behaviour.

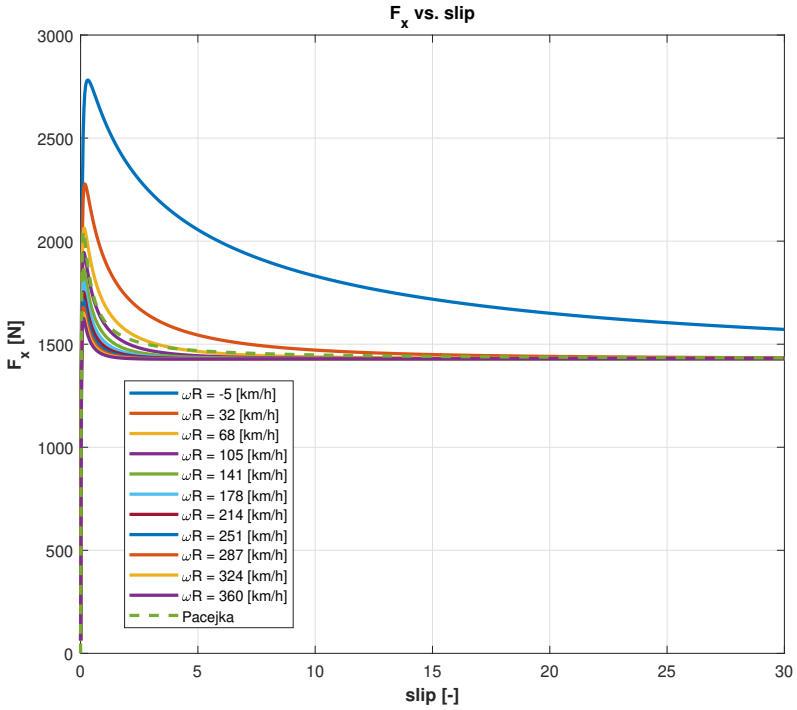

Figure 4.15: Force behaviour for slip values higher than 1.

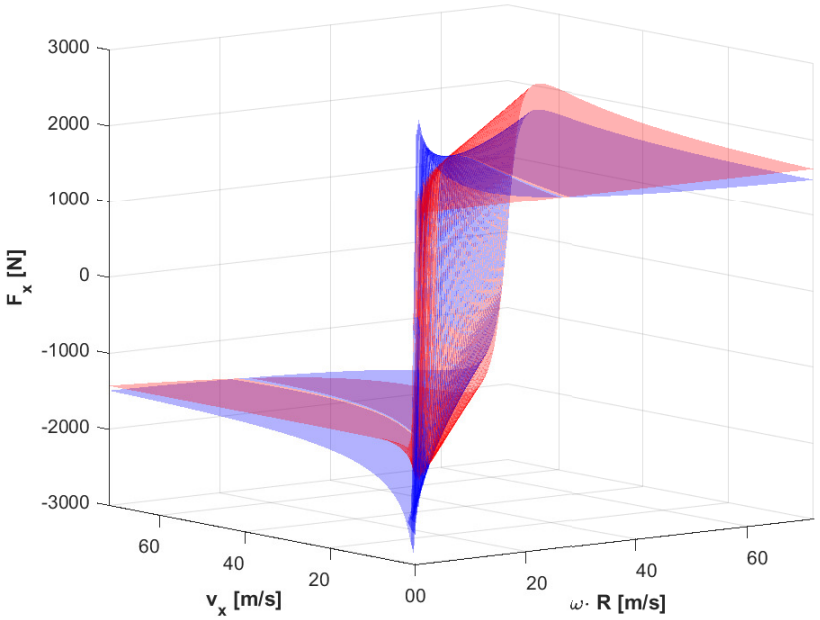

Figure 4.16: Force behaviour after the parameters tuning. In red is the Pacejka force surface and in blue is the LuGre model tyre force behaviour.

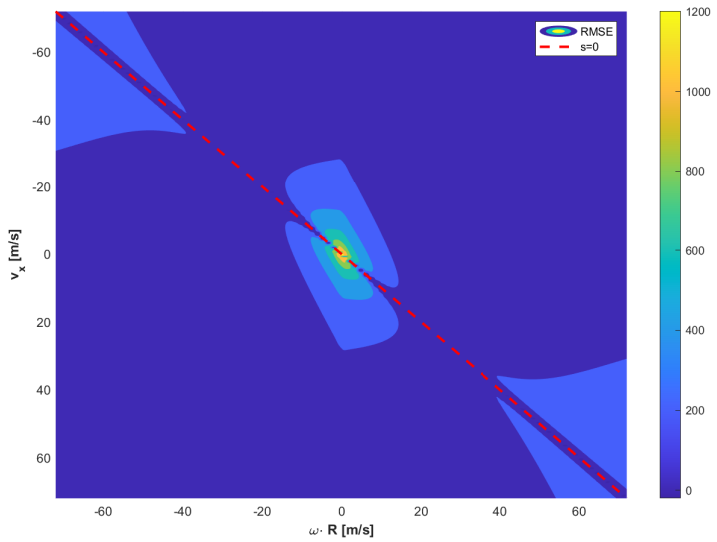

Figure 4.17: RMSE between the LuGre tyre model and the Pacejka one.

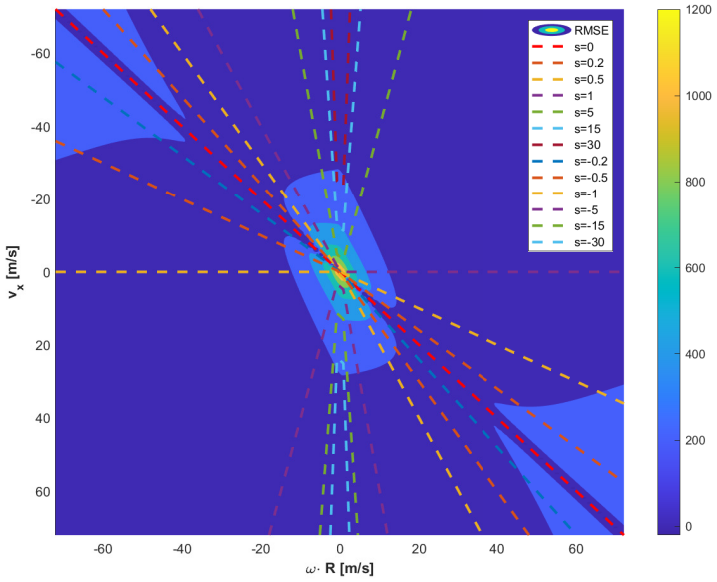

Figure 4.18: RMSE contour with slip values plotted.

4.3 Requirements for tyre testing - model parameters adaptation

Accurately modelling tyre behaviour is crucial for evaluating the impact of different tyre designs on vehicle dynamics. While the speed dependency of the LuGre tyre model has been assessed in section 4.2.4, this phenomenon is not considered in a

semi-empirical tyre model like the Pacejka model. To assess whether the physics of the tyre results in a speed-dependent force, controlled experiments must be conducted. By comparing the results of these experiments with simulation data, the LuGre tyre model can be validated or rejected. Therefore, it is essential to perform such tests under controlled conditions to gain a better understanding of the physics behind tyre behaviour.

Currently, two distinct methods are employed in laboratory settings for the determination of the dynamic performance characteristics of tyres, contingent upon the nature of the tyre rolling surface. These methods include the drum and the flat track type constructions [2, 10]. In this section, we will focus on flat track type as the drum creates an artificial curvature on the contact patch, resulting in a non-representative pressure distribution when compared to actual road conditions [2].

Tyre testing on a flat track machine involves a flat track with a motorized drum that moves a belt to simulate the road surface. The tyre to be tested is mounted on a test wheel and driven on the belt at a specific load, pressure, and speed V (see the sketch of Figure 4.19).

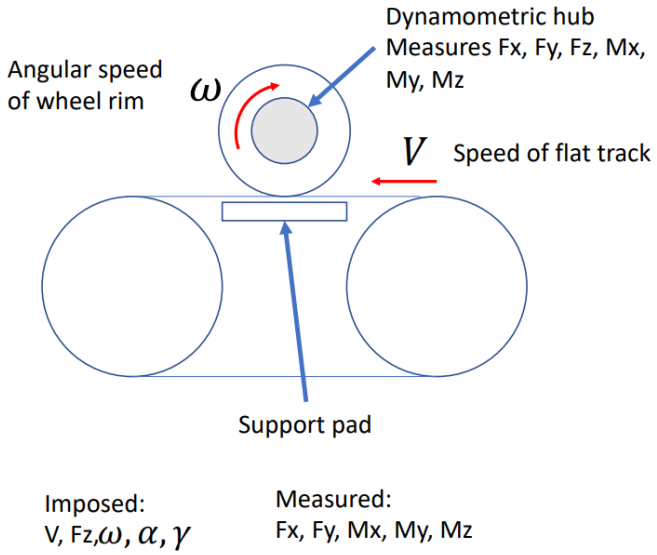

Figure 4.19: Tyre test-track sketch. The dynamometric hub is used to measure the forces arising on the tyre. The tyre is pressed on the belt with a certain F_z, while the belt is turning at a defined longitudinal velocity V imposed by the machine. The angular velocity ω can also make vary to test different slip conditions. Other parameters like the side-slip angle α and the camber angle γ can be imposed to study combined-slip.

During the test, the sensors of the dynamometric hub are used to measure various forces. The data obtained are then processed as the semi-empirical tyre models make use of these data to fit the tyre force equation parameters (refer to (3.3)). The estimation process involves minimizing the error between the experimental data and the tyre model using nonlinear least-squares fitting methods [10].

The LuGre tyre model can still be validated by conducting tests on this flat track machine. However, the testing should involve varying both the angular and longitudinal speeds, denoted by ω and V, respectively. As shown in Figure 4.12, fixing a certain value of slip results in the tyre exhibiting varying levels of forces when the value of ω is altered. However, to maintain a constant slip for different values of ω, the value of V must also be varied accordingly to the slip equation

$$s_x = \frac{\omega \cdot R - V}{|\omega \cdot R|}.$$

One possible approach is to systematically vary the speed of the belt V and the angular speed of the tyre rim ω to maintain a constant value of slip s_x. The process could then be repeated for different values of slips.

Alternatively, a constant belt velocity V can be maintained while varying the angular rim speed ω as done in a normal test. Then the test should be repeated at very different values of V. In fact, the greatest differences in the LuGre tyre model can be appreciated especially if looking at the force level at very low speeds with respect to medium and high speeds (see Figure 4.12).

4.3.1 Damping parameter - σ_1

In section 4.2.4, to compare the LuGre tyre model with the Pacejka model, the tyre force characteristic has been obtained considering the steady-state response of the dynamic tyre model. This means that each point of Figure 4.12, Figure 4.13 and Figure 4.15 represent the steady-state force value for a given speed v_x and angular speed ω. Recalling (4.17), steady-state condition means having

$$\frac{\partial z(\xi, t)}{\partial t} = 0, \tag{4.28}$$

consequently, (4.18) can be expressed as

$$\mu(t, \xi) = \sigma_0 \cdot z(t, \xi) + \sigma_2 \cdot v_r. \tag{4.29}$$

The term $\sigma_1 \cdot \dfrac{\partial z(\xi, t)}{\partial t}$ disappears and σ_1 does not have any influence on the tyre-ground force characteristic when tuning the LuGre parameters to align with the Pacejka model.

However, the damping value σ_1 plays an important role in the tyre force dynamic response. One procedure that could be followed to capture its influence on the tyre behaviour is to use the flat track machine dynamically. Since σ_1 has an influence only in dynamic conditions, the idea is to implement and measure data coming from a torque step input applied to the wheel. In this way, by measuring the tyre force response F_x, it would be possible to determine the tyre damping value. It should be noted that this research does not aim to provide a definitive experimental procedure for tyre testing, but rather to highlight existing issues and suggest potential improvements for future work.

4.4 LuGre tyre model applied to a wheel

To test the LuGre tyre model in the critical condition of $\omega \cdot R = 0$, simulations are performed on an accelerated wheel on a slope of $\alpha = 20$ [deg] as the one in Figure 4.20.

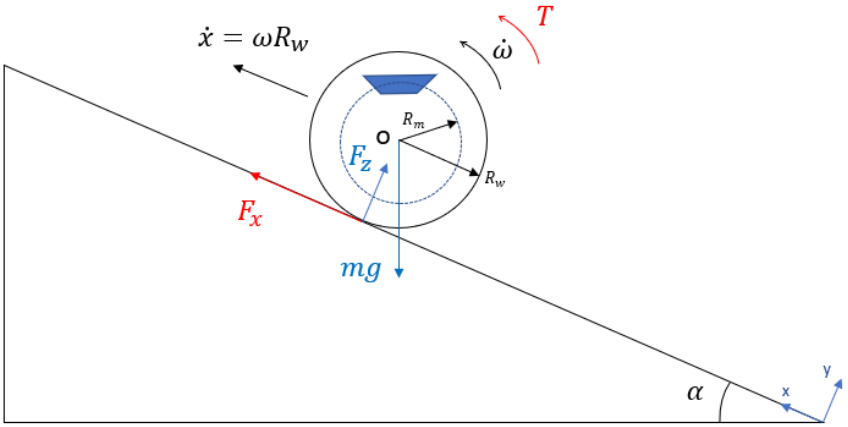

Figure 4.20: Accelerated wheel on a slope.

Here the wheel is going down the slope and a torque is trying to accelerate it in the opposite direction. The equations governing the dynamics of the wheel are shown in (4.30).

$$m \cdot g \cdot \sin(\alpha) - F_x = m \cdot \ddot{x}, \tag{4.30a}$$

$$m \cdot g \cdot \cos(\alpha) - F_z = 0, \tag{4.30b}$$

$$T - F_x \cdot R_w = J_w \cdot \dot{\omega}, \tag{4.30c}$$

$$\frac{\partial z(\xi,t)}{\partial t} = v_r - \frac{\sigma_0 \cdot |v_r|}{g(v_r)} \cdot z(\xi,t) - |\omega \cdot R| \cdot \frac{\partial z(\xi,t)}{\partial \xi}, \tag{4.30d}$$

$$\mu(t,\xi) = \sigma_0 \cdot z(t,\xi) + \sigma_1 \cdot \frac{\partial z(\xi,t)}{,} \partial t + \sigma_2 \cdot v_r \tag{4.30e}$$

$$p(\xi) = \frac{6 \cdot F_z}{L^2} \cdot \xi \cdot (1 - \frac{\xi}{L}), \tag{4.30f}$$

$$F_x(t) = \int_0^L \mu(t,\xi) \cdot p(\xi) \cdot d\xi. \tag{4.30g}$$

A parabolic pressure distribution represents the vertical force exchange between the tyre and the ground. The model made use of the parameters reported in Table 4.5 and the initial conditions for the simulated system are

$$\dot{x}_0 = -1 \text{ [m/s]},$$

$$\dot{\omega}_0 = \frac{\dot{x}_0}{R_w} \text{ [rad/s]}.$$

The applied torque is made to increase from 0 to T_{max} with time t:

$$T = \max(3 \cdot T_{max} \cdot t,\ T_{max}), \qquad \text{subjected to } T_{max} = 200 \text{ [Nm]}. \tag{4.31}$$

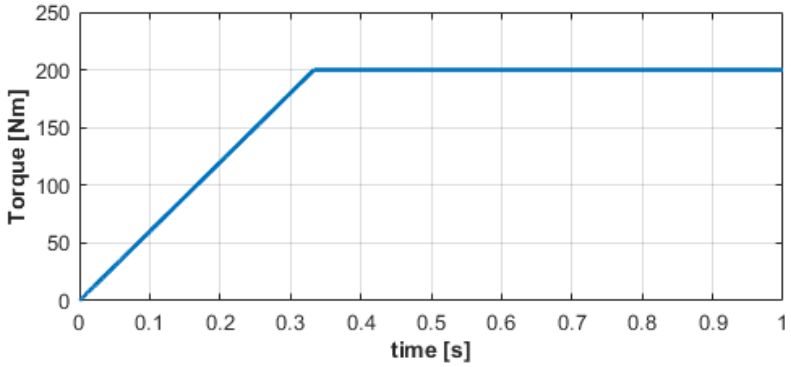

Figure 4.21: Torque input.

The results coming out from the simulation of (4.30) are visible in Figure 4.22. The wheel longitudinal speed correctly increases moving from v_0 up to speeds higher than 0. Moreover, when $\omega \cdot R$ becomes equal to 0 no problems arise in defining the tyre-ground force, contrary to what happens if we consider a slip-based model.

4.5 Interaction between tyre and brake

So far, the effect of the brakes and the behaviour of the tyre have been analyzed separately to understand how to model the real-world friction behaviour and which are the assumptions and the results behind the proposed methods. Nevertheless, in real-world scenarios, the dynamics of brakes and tyres are interrelated. For instance, let us imagine approaching a traffic light and engaging the brakes. The friction between the pads and discs produces a braking torque, while the tyre braking force is determined by both the requested torque and the tyre-ground contact behaviour.

To properly understand how these effects occur together, it is still worthwhile to maintain the problem under investigation simple from the point of view of the physical model. Thus, the model represented in Figure 4.23 will be still used before moving to more realistic vehicle models. The parameter and physical quantities of the wheel are the ones reported in Table 4.1.

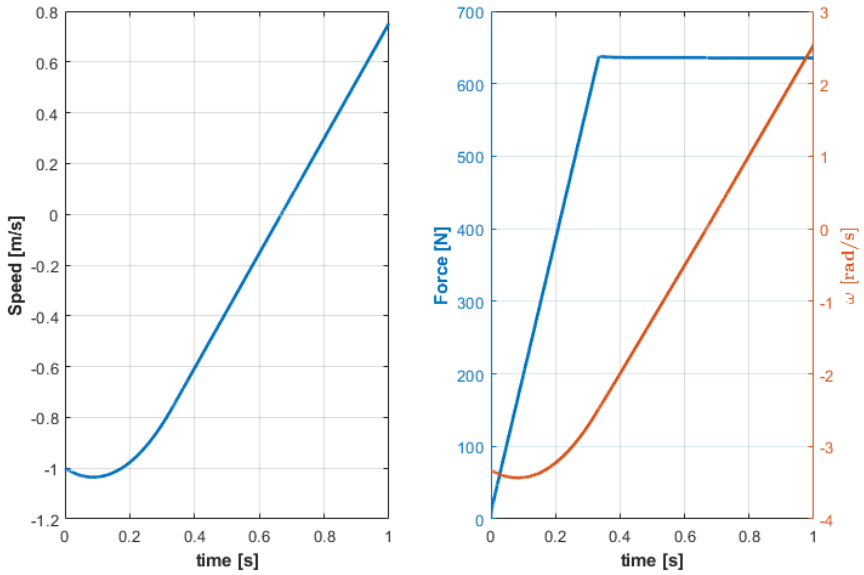

Figure 4.22: Force and speeds of the wheel. The speed initially decreases due to the road slope and the low torque applied. The force behaviour reflects the torque input and correctly saturates when the torque reaches its maximum value T_{max}. Moreover, when ω reaches zero, the force correctly does not change.

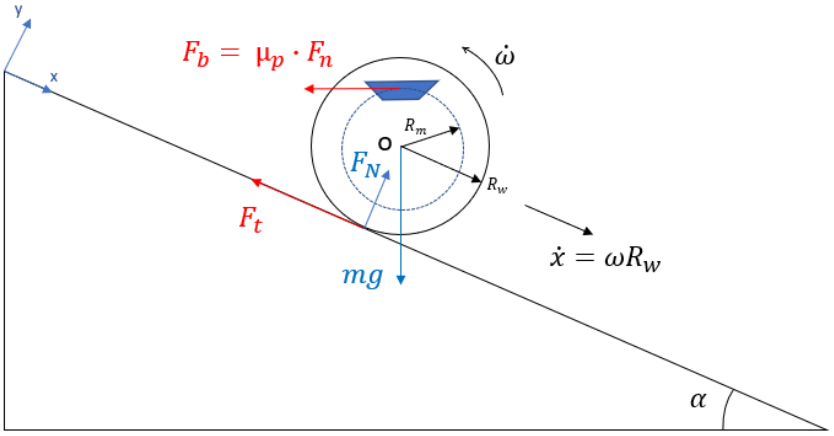

Figure 4.23: Wheel equipped with a disc brake that is braking it to stop the motion.

4.5.1 Brake model

For the purpose of simulations, the elasto-plastic model shown in subsection 4.1.2 has been implemented.

4.5.2 Tyre model

At this point, the non-slipping wheel used in previous simulations will be replaced with the LuGre tyre model, which has been parameterized according to the values presented in Table 4.5. Additionally, to provide a benchmark for comparison, the Pacejka tyre model has also been implemented, with its parameters set to the values presented in Table 4.4. However, to address the singularity issue mentioned in section 1.2, the slip parameter has been opportunely modified by introducing a small constant at the denominator to prevent it from becoming zero, thereby allowing the Pacejka tyre model to function effectively at all speeds, so that (1.6) becomes

$$s_x = \frac{\omega \cdot R - v_x}{\max(\omega \cdot R,\ \ 0.1)}. \tag{4.32}$$

4.5.3 Simulated event

To properly test how the mentioned two effects interact, a braking manoeuvre is implemented. The model is simulated starting from the following initial conditions:

$$\begin{aligned} &\alpha = \text{road slope} = 5 \ \ [\text{deg}], \\ &\dot{x}_0 = 2 \ [\text{m/s}], \end{aligned}$$

$$\dot{\omega}_0 = \frac{\dot{x}_0}{R_w} \ [\text{rad/s}]$$

and recalling (4.2b), the braking torque is actuated by a linearly increasing brake line pressure with time t, as in (4.33).

$$p = \max(10 \cdot p_{max} \cdot t,\ \ p_{max}), \qquad \text{subjected to } \ p_{max} = 10e5 \ \ [\text{Pa}]. \tag{4.33}$$

4.5.4 Results

The analysis of the simulation results presented in this next section provides valuable insights into the behaviour of the LuGre and Pacejka tyre models. In Figure 4.24 (a) and (b) are depicted the acceleration and speed behaviour for the aforementioned models, respectively. Based on the results presented in Figure 4.24(a), the simulations demonstrate that both models exhibit similar behaviour before reaching zero speed, with minor oscillations present in the LuGre tyre model around 0.1 seconds. However, a significant difference is observed at around 0.22 seconds (see Figure 4.25(a)), where a large jerk is exhibited by the Pacejka model due to the brake friction force transitioning from dynamic to static conditions. In contrast, the LuGre model does not exhibit a similar peak, although some minor fluctuations are still present.

This discrepancy can be explained by the fact that the LuGre tyre model is a dynamic model which incorporates the behaviour of the bristles as spring and damper elements. This introduces a force-transmissibility damping effect that filters the

brake dynamics. On the other hand, the Pacejka model is not a dynamic tyre model, so an increase in torque leads to a proportional increase in the tyre-ground force. It is noteworthy that at approximately 0.21 seconds, the Pacejka model experiences a decrease in acceleration (see Figure 4.25(a)). This can be attributed to the use of a modified slip variable, wherein the denominator remains constant while the numerator decreases once the rotational speed falls below 0.1 (see Figure 4.25(b)). A contrasting behaviour is observed at a later instant when the speed reaches zero. In this scenario, the Pacejka tyre model exhibits a sharp decrease in acceleration to zero, while the LuGre tyre model displays oscillations resulting from the spring effect of the bristles.

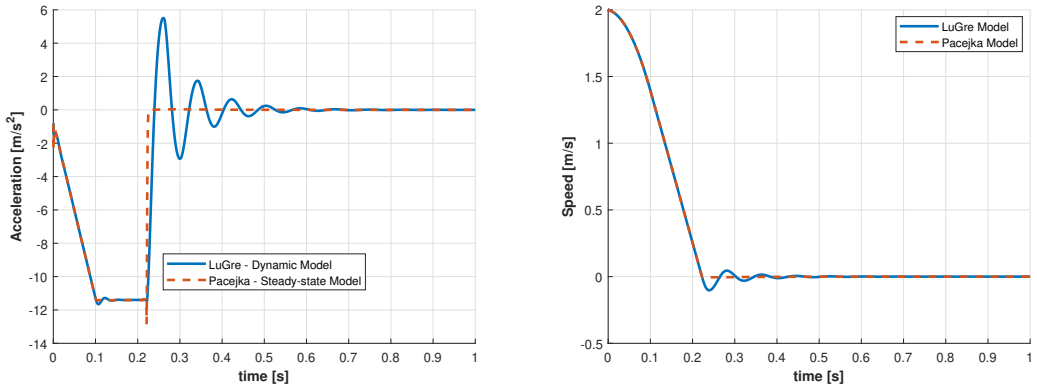

(a) (b)

Figure 4.24: Acceleration (a) and speed (b) trend of the wheel.

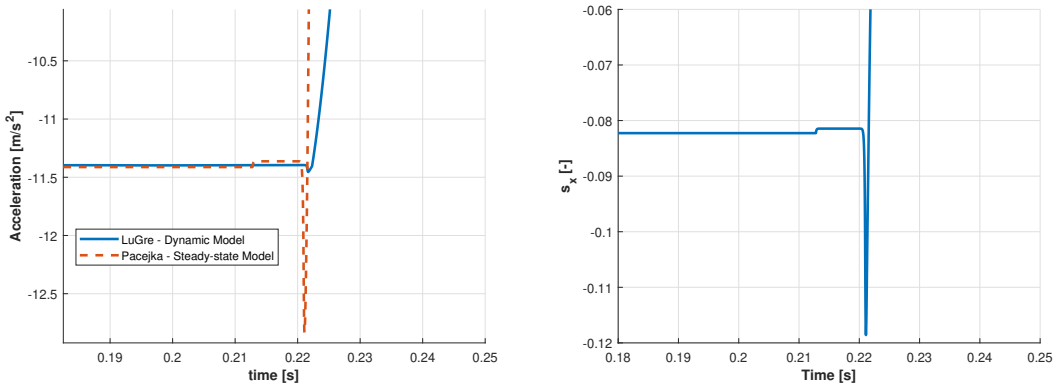

(a) (b)

Figure 4.25: Acceleration (a) and slip (b) behaviour when moving to static friction brake force conditions.

By examining the rate of change of acceleration (that is in fact the **jerk** we want to capture), as shown in Figure 4.26, we can identify some noteworthy characteristics. Specifically, the Pacejka tyre model displays abrupt changes in acceleration as soon

as the braking manoeuvre starts and when the wheel speed reaches zero. This is a non-physical behaviour of the model.

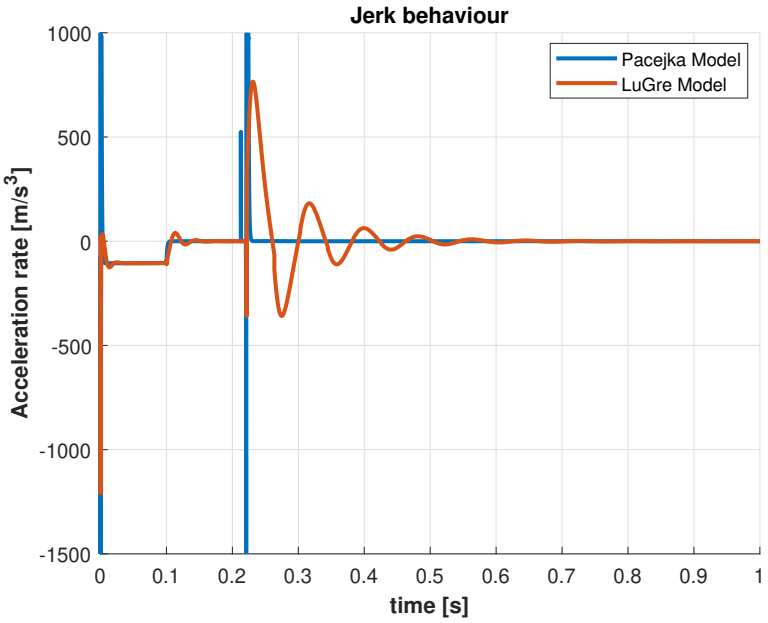

Figure 4.26: Jerk trend of the wheel.

4.6 Remarks

Some conclusions and observations can be extrapolated by the simulation analyzed in section 4.5.4.

- The Pacejka tyre model can work at very low speeds only by using a modified slip variable (4.32). However, this introduces errors when computing forces (and so the accelerations) at very low speeds (0.21 seconds on Figure 4.25(a)).
- The Pacejka model and the LuGre model output different results when the brake force moves from dynamic to static conditions (Figure 4.25(a)). The damping characteristic of the LuGre tyre model is the main reason for this difference (see Figure 4.27). However, it is possible to fine-tune the model to match real-world experimental data (if available).
- The LuGre tyre model shows a more realistic jerk behaviour with respect to the Pacejka one.

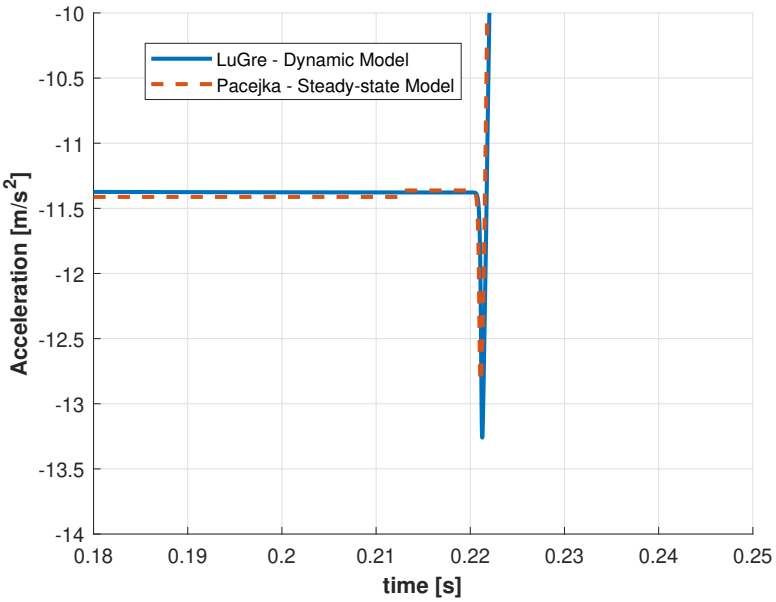

Figure 4.27: Acceleration behaviour when moving to static friction brake force conditions, with a LuGre tyre model damping of $\sigma_1 = 100$ [s/m].

Chapter 5

Jerk on a complete longitudinal vehicle model

So far, what has been done is to develop and analyze friction and tyre models on single components, namely wheels and brake discs. This approach enables the analysis and validation of the aforementioned models under conditions where singularities may arise. However, when applied to a complete vehicle, additional factors may contribute to the occurrence of jerks. Since the vehicle is not a rigid body, compliance elements such as the suspensions must be considered with great care to accurately account for their (possible) effects.

In this chapter different longitudinal vehicle models will be built, starting from a simple 3 degrees of freedom (DOF) rigid vehicle model up to complete featured suspension vehicle models. The models will be developed to simulate the dynamic behaviour of vehicles in the longitudinal direction, specifically in terms of acceleration and deceleration. Therefore, the models considered will be half-car models in which the elements (i.e. wheels and suspensions) of the left and right sides of the vehicle are considered clamped together.

The presence of real vehicle data provides an opportunity to compare the simulated vehicle models with actual results. This allows for a better understanding of the factors that contribute to the jerk effect and the influence of different vehicle components on acceleration and deceleration behaviour. Furthermore, by selectively simplifying the model, such as by removing the suspensions or considering non-slipping wheels, it is possible to identify which elements of the vehicle have the most significant impact on acceleration behaviour.

5.1 Vehicle considered

As mentioned above, real vehicle data will be used for analysis and consideration. The vehicle used to perform real track manoeuvres is a premium SUV that for confidentiality purposes will not be disclosed in this context. All the parameters characterizing the vehicle can be found in Appendix B.

5.2 Rigid longitudinal vehicle model

Starting from the simplest rigid vehicle model the free-body diagram depicted in Figure 5.1 serves as the starting point for the development of the model. It considers only 3 DOF that are represented by the longitudinal displacement of the vehicle and the two angular rotations of the front and rear wheels respectively. From the free-body diagram, we can set up the equilibrium equations for the complete vehicle, so that

$$F_{x,f} + F_{x,r} - m \cdot g \cdot \sin(\alpha) - F_{Aer} = m \cdot \ddot{x}, \tag{5.1a}$$

$$F_{z,f} + F_{z,r} - m \cdot g \cdot \cos(\alpha) = 0, \tag{5.1b}$$

$$\begin{aligned} F_{z,r} \cdot (l_r - \Delta u_r) - F_{z,f} \cdot (l_r + \Delta u_f) - m \cdot g \cdot \sin(\alpha) \cdot h_G + \\ - m \cdot \ddot{x} \cdot h_G - F_{Aer} \cdot h_{Aer} = J_{w,r} \cdot \dot{\omega}_{w,r} + J_{w,f} \cdot \dot{\omega}_{w,f}. \end{aligned} \tag{5.1c}$$

The rotational equilibrium of the wheels (based on the physical model of Figure 5.2) has to be set to calculate their angular velocities and is given by

$$T_{p,f} - |T_{b,f}| - F_{x,f} \cdot R - F_{z,f} \cdot \Delta u_f = J_{w,f} \cdot \dot{\omega}_{w,f}, \tag{5.2a}$$

$$T_{p,r} - |T_{b,r}| - F_{x,r} \cdot R - F_{z,r} \cdot \Delta u_r = J_{w,r} \cdot \dot{\omega}_{w,r}. \tag{5.2b}$$

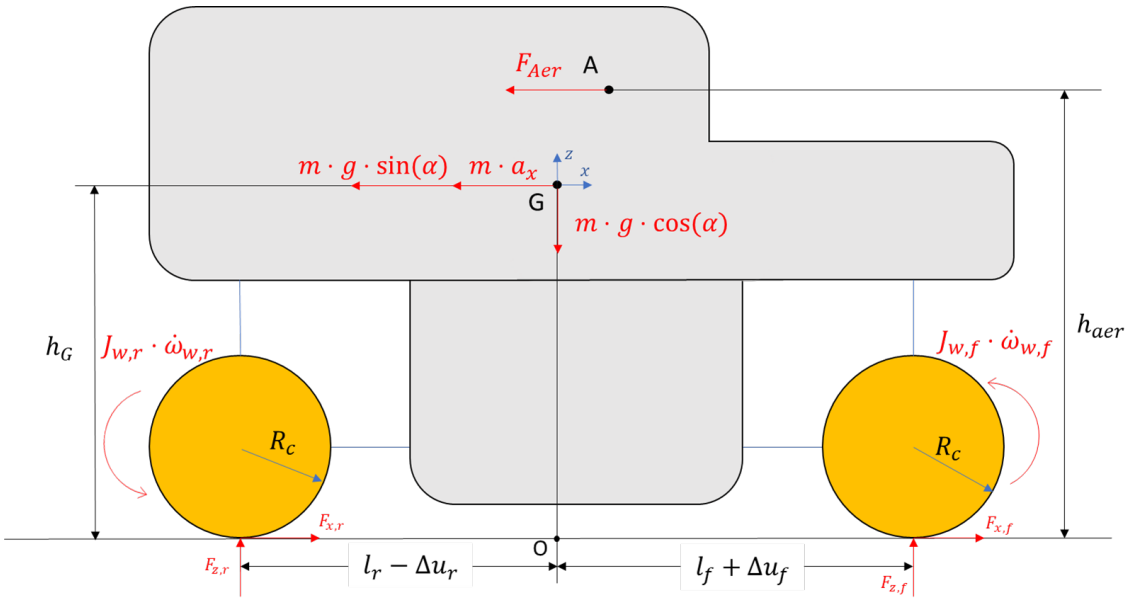

Figure 5.1: Free-body diagram for the SUV rigid vehicle model.

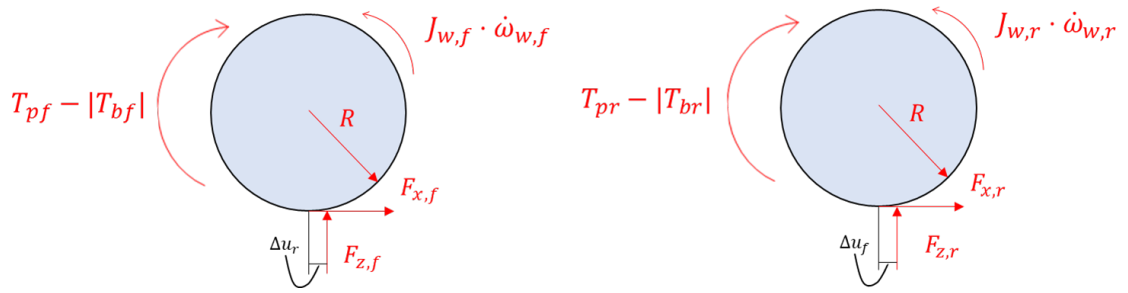

Figure 5.2: Wheel forces contributing to the moment equilibrium of the front and the rear wheels. The terms $T_{p,f}$, $T_{b,f}$, $T_{p,r}$, $T_{b,r}$ represent the propelling and the braking torque applied at the front and rear wheels respectively. Δu represents the rolling resistance coefficient and it is modelled as $\Delta u = K \cdot \dot{x}^2$

5.2.1 Brake modelling

The terms $T_{p,f}$ and $T_{p,r}$ represent the driving torques applied at the front and rear wheels respectively, while $T_{b,f}$ and $T_{b,r}$ represent the corresponding braking torque components. However, as mentioned during the treaty in (4.2b), these braking torques are produced by the friction effect which arises by pushing the brake pads against the brake discs of the wheels. In order to study the behaviour of the model under braking conditions, a braking pressure p_i will be applied at the front and the rear brakes during the simulations. Therefore, it is essential to incorporate a model that can accurately account for the friction effects between the brake pads and discs. Considering the elasto-plastic model presented in section 2.2.2 the braking torque can be computed by

$$T_{b,i} = N_i \cdot R_{m,i} \cdot \mu_b \cdot A_p \cdot p_i, \tag{5.3a}$$

where

$$\dot{z}_b = \omega_i \cdot R - \sigma_0 \cdot \alpha(z_{b,i}, \omega_i \cdot R) \cdot \frac{|\omega_i \cdot R|}{g(\omega_i \cdot R)} \cdot z_{b,i}, \tag{5.3b}$$

$$g(\omega_i \cdot R) = \mu_{d,b} + (\mu_{s,b} - \mu_{d,b}) \cdot e^{-\left(\frac{|\omega_i \cdot R|}{v_{s,b}}\right)^{\alpha_b}}, \tag{5.3c}$$

$$\mu_b = \sigma_{0,b} \cdot z_{b,i} + \sigma_{1,b} \cdot \dot{z}_{b,i} + \sigma_{2,b} \cdot \dot{\omega}_i \cdot R, \tag{5.3d}$$

where the subscript i indicates a general wheel (either front or rear), while the subscript b denotes that the parameters are related to the brake and N_i indicates the number of brake cylinders in the i-th wheel braking disc.

5.2.2 Tyre modelling

For the i^{th} wheel, calling $T_{tot,i}$ the sum of the external torques applied at the wheel (i.e. propelling, braking, rolling resistance, etc.), (5.2) can be re-written as

$$T_{tot,i} - F_{x,i} \cdot R = J_{w,i} \cdot \dot{\omega}_{w,i}, \tag{5.4a}$$

where $F_{x,i}$ can be computed, considering the LuGre tyre model as shown in (4.20), to be

$$g(v_{r,i}) = \mu_{d,t} + (\mu_{s,t} - \mu_{d,t}) \cdot e^{-\left(\frac{|v_{r,i}|}{v_{s,t}}\right)^{\alpha_t}}, \tag{5.4b}$$

$$\frac{\partial z_i(\xi_i, t)}{\partial t} = v_{r,i} - \frac{\sigma_0 \cdot |v_{r,i}|}{g(v_{r,i})} \cdot z_i(\xi_i, t) - |\omega_i \cdot R| \cdot \frac{\partial z_i(\xi_i, t)}{\partial \xi_i}, \tag{5.4c}$$

$$\mu_i(t, \xi_i) = \sigma_0 \cdot z(t, \xi_i) + \sigma_1 \cdot \frac{\partial z_i(\xi_i, t)}{\partial t} + \sigma_2 \cdot v_{r,i}, \tag{5.4d}$$

$$p(\xi_i) = \frac{6 \cdot F_{z,i}}{L^2} \cdot \xi_i \cdot (1 - \frac{\xi_i}{L}), \tag{5.4e}$$

$$F_{x,i}(t) = \int_0^L \mu_i(t, \xi_i) \cdot p(\xi_i) \cdot d\xi_i. \tag{5.4f}$$

5.3 Longitudinal vehicle model featuring trivial suspensions

A further useful step in modelling is represented by the implementation of the suspensions. We propose the model depicted in Figure 5.3. It distinguishes between the *unsprung mass* m_u (which includes the wheels and the non-heaving part of the suspension) and the *sprung mass* m_s or body (which includes the parts that heave and pitch as a single rigid body). Because of this distinction, we can consider these masses separated, with each of them having its own centre of gravity (CoG). The vehicle body CoG will be indicated with G_s, while the CoGs of the front and rear unsprung masses will be denoted with $G_{u,r}$ and $G_{u,f}$, respectively. In this model, the wheels are connected to the body through a *trivial linkage* and a flat ground is assumed, resulting in a zero vertical displacement of the unsprung mass. The centre of gravity of the unsprung masses is considered to be positioned in the centre of the wheels. From the free-body diagram, we can set up the equilibrium equations for the complete vehicle as in (5.5). Due to the introduction of the pitch motion of the sprung mass, since forces and accelerations are expressed in the body reference frame of the vehicle, the centrifugal terms $\omega_y \cdot \dot{z}_s$ and $\omega_y \cdot \dot{x}$ appear in the inertia force terms of the longitudinal and vertical equilibrium respectively.

$$\begin{aligned} F_{x,f} + F_{x,r} - (m_s + m_{u,r} + m_{u,f}) \cdot g \cdot \sin(\alpha) - F_{Aer} = \\ = m_s \cdot (\ddot{x} + \omega_y \cdot \dot{z}_s) + m_{u,f} \cdot \ddot{x} + m_{u,r} \cdot \ddot{x}, \end{aligned} \tag{5.5a}$$

$$F_{z,f} + F_{z,r} - (m_s + m_{u,r} + m_{u,f}) \cdot g \cdot \cos(\alpha) = m_s \cdot (\ddot{z}_s - \omega_y \cdot \dot{x}), \tag{5.5b}$$

$$\begin{aligned} &F_{z,r} \cdot (l_r - \Delta u_r) - F_{z,f} \cdot (l_r + \Delta u_f) - (m_s + m_{u,r} + m_{u,f}) \cdot g \cdot \sin(\alpha) \cdot h_G + \\ &- m_s \cdot (\ddot{x} + \omega_y \cdot \dot{z}_s) \cdot h_{G_s} - m_{u,f} \cdot \ddot{x} \cdot R - m_{u,r} \cdot \ddot{x} \cdot R - F_{Aer} \cdot h_{Aer} = \\ &= J_y \cdot \dot{\omega}_{y,s} + J_{w,r} \cdot \dot{\omega}_{w,r} + J_{w,f} \cdot \dot{\omega}_{w,f}. \end{aligned} \tag{5.5c}$$

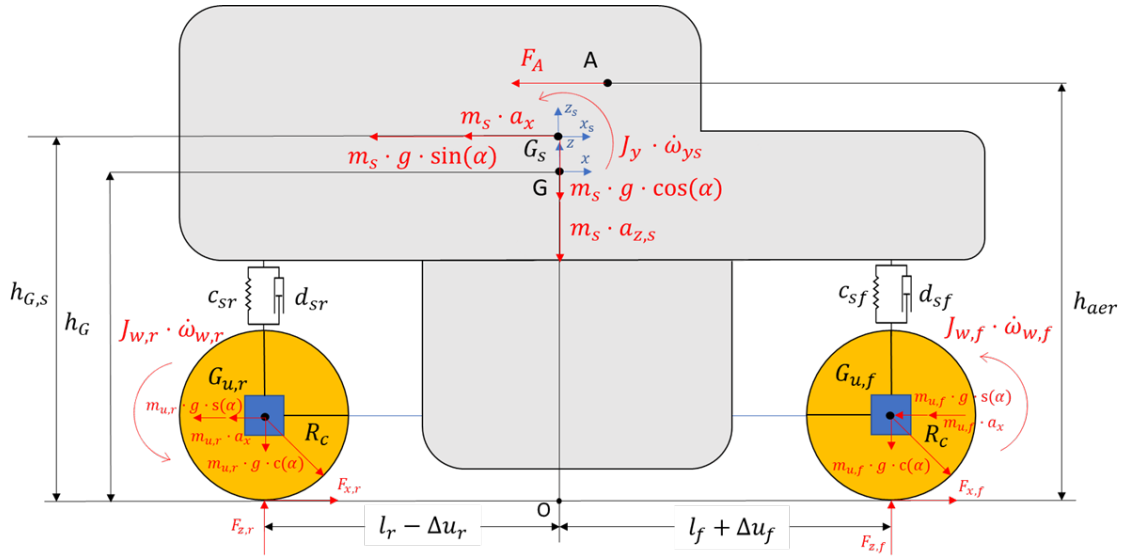

Figure 5.3: Free-body diagram for the SUV model featured with suspensions. In this model, the wheels are connected to the body through a *trivial linkage*, meaning that the actual pivot point of the suspension is not considered, but the wheels exchange force with sprung mass only by the spring and the damper of the suspensions.

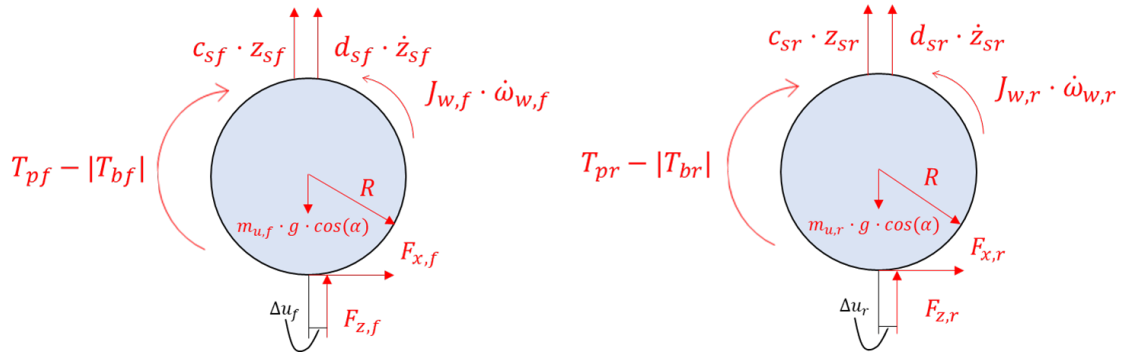

Figure 5.4: Wheel forces contributing to the moment and the vertical equilibrium of the front and the rear wheels.

The vertical equilibrium of the wheels (based on the physical model of Figure 5.4) leads to

$$F_{z,f} - m_{u,f} \cdot g \cdot \cos(\alpha) + c_{s,f} \cdot z_{s,f} + d_{s,f} \cdot \dot{z}_{s,f} = 0, \tag{5.6a}$$

$$F_{z,r} - m_{u,r} \cdot g \cdot \cos(\alpha) + c_{s,r} \cdot z_{s,r} + d_{s,r} \cdot \dot{z}_{s,r} = 0, \tag{5.6b}$$

with the compatibility equations, to connect the body CoG displacements to the body suspension attachments, given by

$$z_{s,f} = z_s - \phi_{y,s} \cdot l_f, \tag{5.6c}$$

$$z_{s,r} = z_s + \phi_{y,s} \cdot l_r, \tag{5.6d}$$

$$\dot{z}_{s,f} = \dot{z}_s - \omega_{y,s} \cdot l_f, \tag{5.6e}$$

$$\dot{z}_{s,r} = \dot{z}_s + \omega_{y,s} \cdot l_r, \tag{5.6f}$$

where

$$\dot{\phi}_{y,s} = \omega_{y,s}. \tag{5.6g}$$

The rotational equilibrium of the wheels (based on the physical model of Figure 5.4) has to be set to calculate their angular velocities and is formulated as

$$T_{p,f} - |T_{b,f}| - F_{x,f} \cdot R - F_{z,f} \cdot \Delta u_f = J_{w,f} \cdot \dot{\omega}_{w,f}, \tag{5.7a}$$

$$T_{p,r} - |T_{b,r}| - F_{x,r} \cdot R - F_{z,r} \cdot \Delta u_r = J_{w,r} \cdot \dot{\omega}_{w,r}, \tag{5.7b}$$

The brake and tyre models are made of the same equations as depicted in (5.3) and (5.4).

5.4 Longitudinal vehicle featuring suspensions and horizontal suspension compliance

Up to this point, the vehicle modelling has focused mainly on the vertical behaviour of the suspension system, neglecting the effects of horizontal suspension and linkages compliance. However, it is beneficial to consider these effects when modelling the longitudinal behaviour of a vehicle, as they could play a significant role in determining the vehicle acceleration and braking performance. In this context, as experimental data are not available, this horizontal compliance has been modelled as a parallel connection of a spring and damper with a stiffness value which is ten times higher than the suspension one (the same values are considered for the front and the rear suspensions). The free-body diagram of the model can be seen in Figure 5.5. From the FBD, the set of equations characterizing the physical vehicle model are reported in (5.8) given by

$$\begin{aligned} F_{x,f} + F_{x,r} - (m_s + m_{u,r} + m_{u,f}) \cdot g \cdot \sin(\alpha) - F_{Aer} = \\ = m_s \cdot (\ddot{x} + \omega_y \cdot \dot{z}_s) + m_{u,f} \cdot \ddot{x}_f + m_{u,r} \cdot \ddot{x}_r, \end{aligned} \tag{5.8a}$$

$$F_{z,f} + F_{z,r} - (m_s + m_{u,r} + m_{u,f}) \cdot g \cdot \cos(\alpha) = m_s \cdot (\ddot{z}_s - \omega_y \cdot \dot{x}), \tag{5.8b}$$

$$\begin{aligned} &F_{z,r} \cdot (l_r - \Delta u_r) - F_{z,f} \cdot (l_r + \Delta u_f) - (m_s + m_{u,r} + m_{u,f}) \cdot g \cdot \sin(\alpha) \cdot h_G + \\ &- m_s \cdot (\ddot{x} + \omega_y \cdot \dot{z}_s) \cdot h_{G_s} - m_{u,f} \cdot \ddot{x}_f \cdot R - m_{u,r} \cdot \ddot{x}_r \cdot R - F_{Aer} \cdot h_{Aer} = \\ &= J_y \cdot \dot{\omega}_{y,s} + J_{w,r} \cdot \dot{\omega}_{w,r} + J_{w,f} \cdot \dot{\omega}_{w,f}. \end{aligned} \tag{5.8c}$$

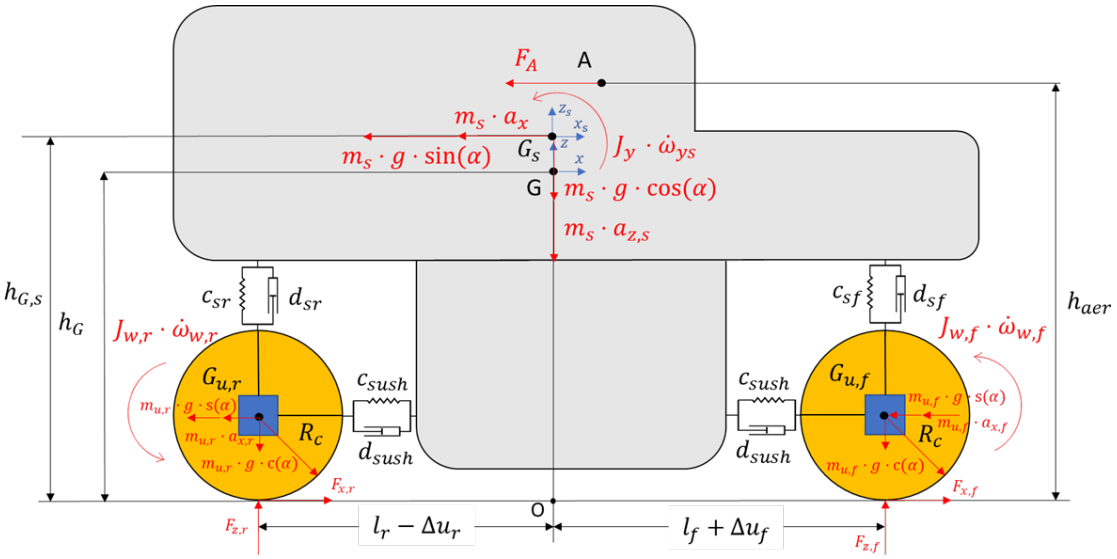

Figure 5.5: Free-body diagram for the SUV model featured with suspensions. The horizontal compliance has been modelled as a parallel connection of a spring and damper both at the front and at the rear.

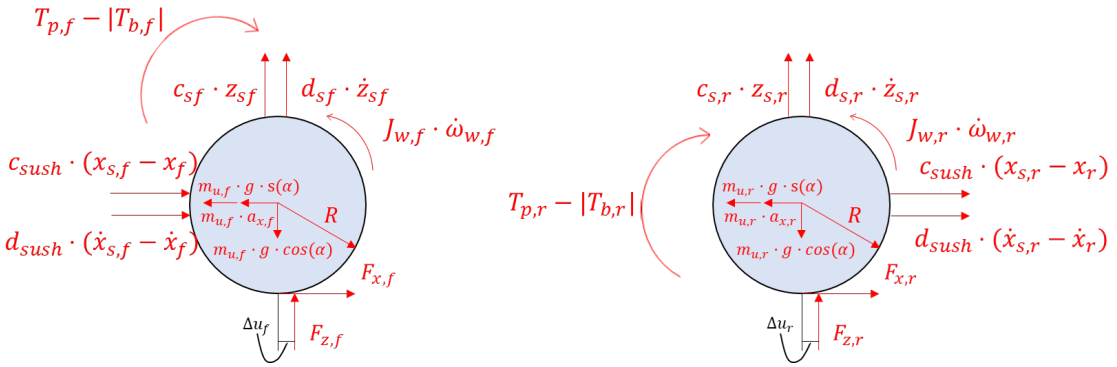

Figure 5.6: Wheel forces contributing to the moment, the horizontal and the vertical equilibrium of the front and the rear wheels.

The horizontal and the vertical equilibrium of the wheels (based on the physical model of Figure 5.6) leads to (5.9) given by

$$F_{x,f} + c_{sush,f} \cdot (x_{s,f} - x_f) + d_{sush,f} \cdot (\dot{x}_{s,f} - \dot{x}_f) - m_{u,f} \cdot g \cdot \sin(\alpha) = m_{u,f} \cdot \ddot{x}_f, \quad (5.9a)$$

$$F_{x,r} + c_{sush,r} \cdot (x_{s,r} - x_r) + d_{sush,r} \cdot (\dot{x}_{s,r} - \dot{x}_r) - m_{u,r} \cdot g \cdot \sin(\alpha) = m_{u,r} \cdot \ddot{x}_r, \quad (5.9b)$$

$$F_{z,f} - m_{u,f} \cdot g \cdot \cos(\alpha) + c_{s,f} \cdot z_{s,f} + d_{s,f} \cdot \dot{z}_{s,f} = 0, \quad (5.9c)$$

$$F_{z,r} - m_{u,r} \cdot g \cdot \cos(\alpha) + c_{s,r} \cdot z_{s,r} + d_{s,r} \cdot \dot{z}_{s,r} = 0. \quad (5.9d)$$

To ensure compatibility, we can establish a relationship between the displacements of the body centre of gravity and the suspension attachment points on the body through

$$x_{s,f} = x_s - (h_{G_s} - R) \cdot \phi_{y,s}, \tag{5.9e}$$

$$x_{s,r} = x_s - (h_{G_s} - R) \cdot \phi_{y,s}, \tag{5.9f}$$

$$\dot{x}_{s,f} = \dot{x}_s - (h_{G_s} - R) \cdot \omega_{y,s}, \tag{5.9g}$$

$$\dot{x}_{s,r} = \dot{x}_s - (h_{G_s} - R) \cdot \omega_{y,s}, \tag{5.9h}$$

$$z_{s,f} = z_s - \phi_{y,s} \cdot l_f, \tag{5.9i}$$

$$z_{s,r} = z_s + \phi_{y,s} \cdot l_r, \tag{5.9j}$$

$$\dot{z}_{s,f} = \dot{z}_s - \omega_{y,s} \cdot l_f, \tag{5.9k}$$

$$\dot{z}_{s,r} = \dot{z}_s + \omega_{y,s} \cdot l_r, \tag{5.9l}$$

and

$$\dot{\phi}_{y,s} = \omega_{y,s}. \tag{5.9m}$$

The rotational equilibrium of the wheels (based on the physical model of Figure 5.6) has to be set to calculate their angular velocities such that

$$T_{p,f} - |T_{b,f}| - F_{x,f} \cdot R - F_{z,f} \cdot \Delta u_f = J_{w,f} \cdot \dot{\omega}_{w,f}, \tag{5.10a}$$

$$T_{p,r} - |T_{b,r}| - F_{x,r} \cdot R - F_{z,r} \cdot \Delta u_r = J_{w,r} \cdot \dot{\omega}_{w,r}. \tag{5.10b}$$

The brake and tyre models are made of the same equations as depicted in Equation 5.3 and Equation 5.4.

5.5 Tyre carcass compliance

In the previous sections, we modelled the longitudinal dynamics of a vehicle, including the tyre *slip* dynamics, the braking system, and the suspension systems. However, these models did not account for the compliance of the tyre carcass, which can have a significant impact on the overall behaviour of the vehicle. In this section, we will consider the compliance of the tyre carcass and its effect on the longitudinal dynamics of the vehicle. Specifically, we will examine how the compliance of the tyre carcass affects the forces and moments acting on the vehicle, and how it can be incorporated into the overall vehicle model. The physical free-body diagram shown in Figure 5.7 can be used to model the exchange of force between the rubber part of the tyre and the rim during acceleration changes. This model takes into account the inertia of both the rim and the belt. Starting from Figure 5.7 and considering a generic tyre i, the mathematical model describing a flexible tyre sidewall can be written as in the system of equations 5.11.

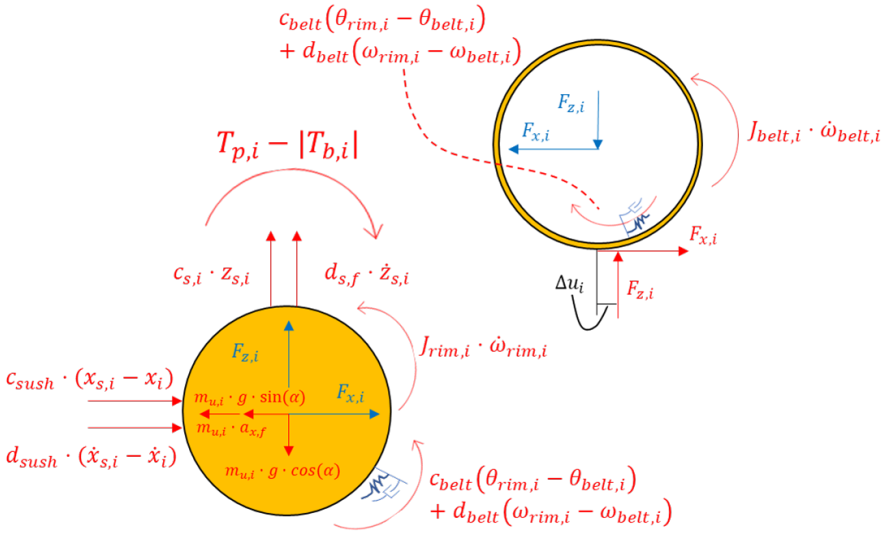

Figure 5.7: The tyre model considered, to incorporate the elasticity of the sidewalls during transient manoeuvres.

Rim horizontal equilibrium:

$$F_{x,i} + c_{sush,i} \cdot (x_{s,i} - x_i) + d_{sush,i} \cdot (\dot{x}_{s,i} - \dot{x}_i) - m_{u,i} \cdot g \cdot \sin(\alpha) = m_{u,i} \cdot \ddot{x}_i \quad (5.11a)$$

Rim vertical equilibrium:

$$F_{z,i} - m_{u,i} \cdot g \cdot \cos(\alpha) + c_{s,i} \cdot z_{s,i} + d_{s,i} \cdot \dot{z}_{s,i} = 0 \quad (5.11b)$$

Rim rotational equilibrium:

$$T_{p,i} - |T_{b,i}| - c_{belt,i} \cdot (\theta_{rim,i} - \theta_{belt,i}) - d_{belt,i} \cdot (\omega_{rim,i} - \omega_{belt,i}) = J_{rim,i} \cdot \dot{\omega}_{rim,i} \quad (5.11c)$$

Belt rotational equilibrium:

$$c_{belt,i} \cdot (\theta_{rim,i} - \theta_{belt,i}) + d_{belt,i} \cdot (\omega_{rim,i} - \omega_{belt,i}) - F_{x,i} \cdot R - F_{z,i} \cdot \Delta u_i = J_{belt,i} \cdot \dot{\omega}_{belt,i} \quad (5.11d)$$

Chapter 6

Simulation set-up: inputs, method and results

As previously stated, the availability of experimental data from actual vehicle tests presents a valuable opportunity to verify the accuracy of the mathematical vehicle model. By using the information on the driver's inputs during the tests, it becomes possible to precisely replicate the same manoeuvre in the simulation environment.

MATLAB©/Simulink© has been used to implement the models presented in the previous chapter. The inputs of the simulations are represented by the acceleration torque commanded by the driver (what was previously called T_p) and the braking pressure applied by pressing the brake pedal (the variable p in (5.3)). These signals were obtained from the aforementioned experimental tests, detailed in subsequent sections.

6.1 Method of analysis

To gain insight into the factors that most significantly contribute to the longitudinal jerk behaviour of a vehicle, the vehicle models described earlier will undergo a testing procedure that involves the following simulation set-up:

1. Rigid vehicle model and non-slipping wheels (that means $\omega \cdot R = \dot{x}$).
2. Rigid vehicle model and slipping wheels.
3. Vehicle model featuring suspensions and non-slipping wheels.
4. Vehicle model featuring suspensions and slipping wheels.
5. Vehicle model featuring suspensions, linkage horizontal compliance and non-slipping wheels.
6. Vehicle model featuring suspensions, linkage horizontal compliance and slipping wheels.
7. Vehicle model without suspensions, with linkage horizontal compliance and slipping wheels.
8. Vehicle model featuring suspensions, linkage horizontal compliance, tyre sidewall dynamics and slipping wheels.

6.2 Braking manoeuvre on asphalt

The first manoeuvre considered is represented by a braking manoeuvre performed after a single-lane change (see Figure 6.1). The vehicle was equipped with an inertia measurement unit (IMU) and an Oxford Instrument RT3000 (OTS), which is a high-precision device which measures motion entities. The logged data of our interest retrieved after the test are:

- Longitudinal acceleration.
- Longitudinal speed.
- Lateral acceleration to ensure the validity of the longitudinal model.
- Tractive torque at the four wheels.
- Braking pressure at the four-wheel lines.
- Wheels angular speeds.

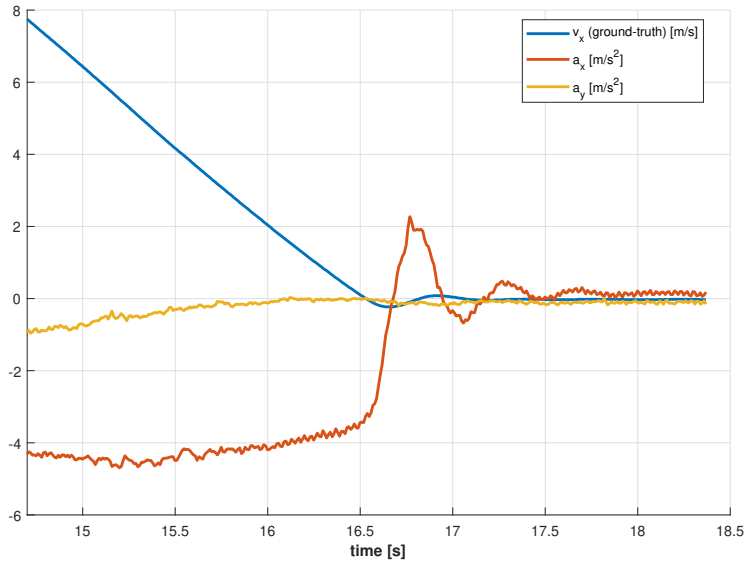

Figure 6.1: Acceleration and speed behaviour during the braking manoeuvre.

6.2.1 Results of the simulation

The results of the longitudinal braking manoeuvre simulations for different types of vehicles are here presented. The plot of Figure 6.2 shows the acceleration profiles of the different mathematical models of vehicles previously introduced.

The acceleration behaviour of the rigid vehicle model with non-slipping wheels can be observed by examining Figure 6.2, where it is represented by the dark orange line (partially obscured by the purple line). We can see that this model is capable of simulating scenarios where the speed reaches zero, and the simulation proceeds smoothly. However, it is important to note that a rigid vehicle model without tyre slip cannot account for acceleration oscillations since it lacks compliance modelling.

Modelling suspensions without accounting for wheel slip does not lead to substantial enhancements in the longitudinal behaviour of the vehicle (see the purple plot on Figure 6.2). The main effect of the suspensions becomes important when the vertical dynamic is analyzed. For the longitudinal dynamics, even if the suspensions do introduce a small longitudinal effect due to the centrifugal term $\omega_y \cdot \dot{z}_s$, this contribution is negligible when examining the overall longitudinal behaviour of the vehicle.

Moving on to the rigid vehicle model with the tyre slip introduced, some oscillations arise due to the presence of spring elements in the bristle tyre dynamics (yellow line on Figure 6.2). As for the previous case, the introduction of suspensions does not change the main behaviour of the model for the reasons stated above (green line on Figure 6.2). Only considering the tyre tread dynamics is also insufficient to accurately capture the real behaviour of the vehicle, as the oscillations occur at different frequencies, although the amplitude is already significant.

We will now focus on the vehicle model without suspensions and without slipping wheels, but with the compliance of the suspension attachments introduced (light blue line on Figure 6.2). The acceleration behaviour of this model reflects quite accurately the experimental data coming from the braking manoeuvre. Additionally, when we incorporate the effects of slipping wheels in the model (red line on Figure 6.2), we observe a further improvement in the model dynamic behaviour.

Incorporating the suspension models into the analysis results in a slight reduction in acceleration peaks, likely due to the load transfer dynamics.

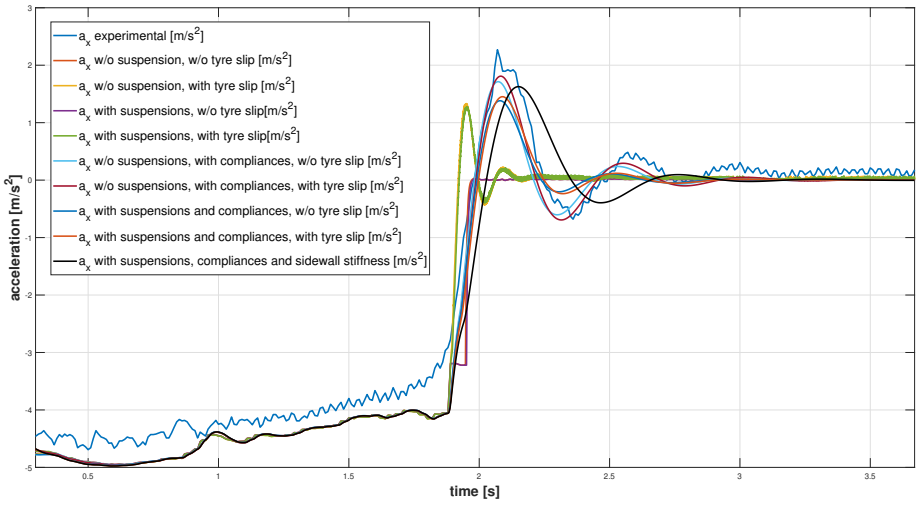

Figure 6.2: Acceleration behaviour during the braking manoeuvre of the different vehicle models.

Particular attention must be paid to the model that handles the tyre sidewall compliance. Plausible values of

$$c_{belt} = 40 \cdot 10^3 \quad [\text{Nm/rad}]$$

and

$$d_{belt} = 2 \cdot 10^3 \quad [\text{Nms/rad}]$$

were assumed for simulation purposes, as actual values were not available. However, variations in stiffness and damping significantly impact acceleration behaviour. Therefore, the trend shown in Figure 6.2 (black plot) seems to yield accurate results, but a more precise analysis is possible only with the precise knowledge of the real tyre stiffness and damping values.

6.2.2 Braking manoeuvre on a slippery surface

The second manoeuvre considered is still represented by a braking manoeuvre, but this time performed on a slippery surface (see Figure 6.3).

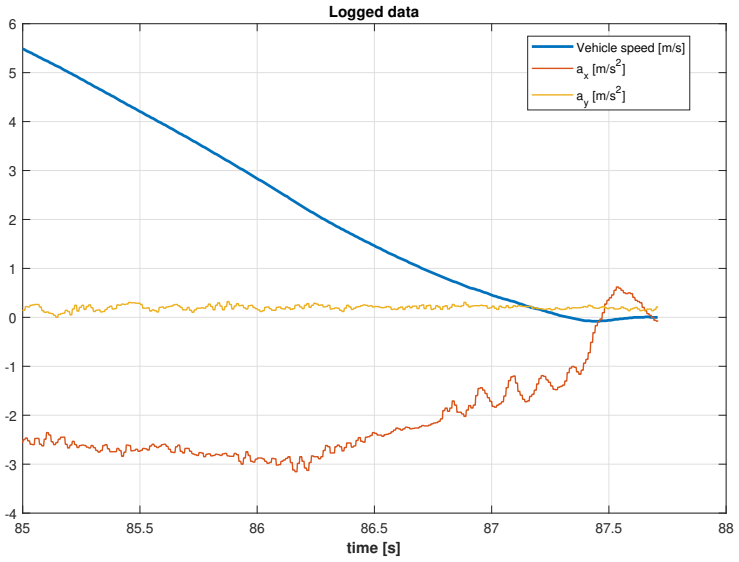

Figure 6.3: Acceleration and speed behaviour during the braking manoeuvre performed on a slippery surface.

Recalling (5.4), to introduce the tyre-ground friction in the model, (5.4b) has been modified as

$$g(\omega_i \cdot R) = \mu_{road} \cdot \left[\mu_d + (\mu_s - \mu_d) \cdot e^{-\left(\frac{|\omega_i \cdot R|}{v_s}\right)^{\alpha}} \right] \tag{6.1}$$

with

$$\mu_{road} = \text{ road friction coefficient} = 0.4$$

that models the reduction of friction on slippery surfaces.

6.2.3 Results of the simulation

As for the previous test case (see section 6.2), the results of the longitudinal braking manoeuvre simulations for different types of vehicles are here presented and shown in Figure 6.4.

Similar considerations to ones made in section 6.2 hold. The rigid vehicle model with non-slipping wheels can simulate deceleration scenarios up to zero speed, but because of its lack of compliance modelling, it cannot mimic the real-world acceleration oscillations. Modelling suspensions without wheel slip does not substantially improve the longitudinal behaviour, except for vertical dynamics. The rigid vehicle model with tyre slip introduces oscillations due to spring elements in the tyre dynamics, while the introduction of suspensions has minimal impact. Considering only tyre tread dynamics (yellow plot) is insufficient to capture the real behaviour accurately. The vehicle model without suspensions but with suspension attachment compliance accurately reflects experimental braking data. Incorporating slipping wheels further improves the dynamic behaviour. The model with tyre sidewall compliance introduces a small drift with respect to the other models. As said it requires precise knowledge of stiffness and damping values, which significantly impact acceleration behaviour.

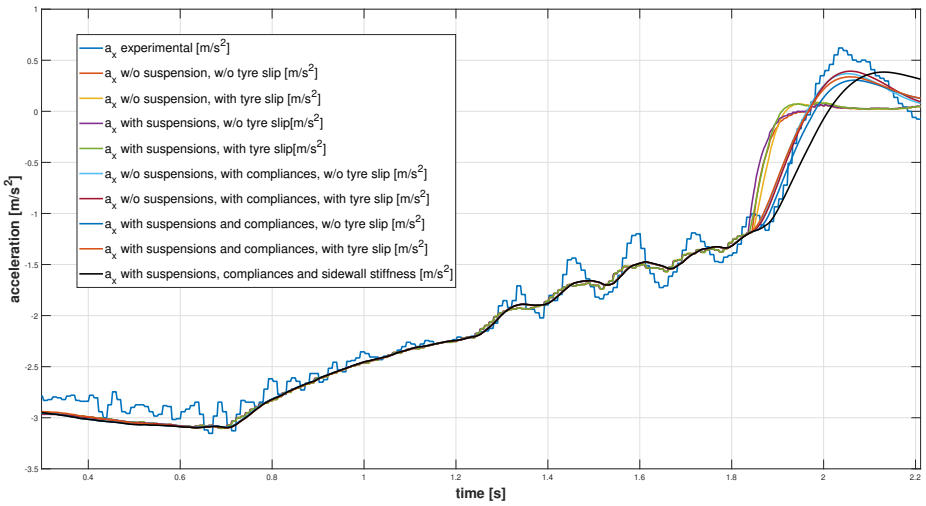

Figure 6.4: Acceleration behaviour during the braking manoeuvre of the different vehicle models.

Chapter 7

Future work

In this chapter, we will explore potential enhancements to the LuGre tyre model and discuss future improvements that can enhance vehicles' acceleration dynamics for comfort and safety. First, a review of the limits of the implemented LuGre tyre model will be given. Subsequently, some necessary requirements to capture the acceleration oscillations in real-world experiments will be investigated and finally, some hints on how to deal with these oscillations to enhance comfort will be discussed.

7.1 Limits of the LuGre tyre model

As already discussed in section 4.2.3, knowledge derived from physical tyre models indicates that the deflection of the bristles should initially increase. However, after reaching a peak value around the peak vertical load, it should decrease to zero at the trailing edge of the contact patch (see Figure 4.11) [9]. The LuGre tyre model fails to replicate this behaviour due to two main reasons:

- The friction term (4.13) in the LuGre model considers the overall relative speed v_r instead of the individual relative speeds between each bristle tip and the ground contact point.
- The saturation condition (4.12) in the LuGre model does not take into account the vertical load, resulting in the deformation being only dependent on the relative speed between the belt and the ground, regardless of the applied vertical force (even if it is zero).

Addressing these issues may require improvements in the models, potentially involving the use of non-linear differential equations. However, it is important to investigate the trade-off between complexity and precision of the results, considering that the current model already provides accurate simulation behaviours. Additionally, it is worth noting that the focus is typically on the final force effect rather than tread deformation.

7.2 Requirements to capture Jerk

Although we have examined outcomes within the domain of simulations, it is essential to specify that real-world testing and measurements of physical phenomena require the use of instruments and sensors, like an Inertia Measurement Unit (IMU), with specific resolutions and precision. In this context, capturing jerk, which is the rate of change of acceleration, is particularly challenging due to the limitations of these instruments.

One critical consideration in capturing jerk is the sampling time of the instruments and sensors. The sampling time refers to the frequency at which the device takes measurements. If the sampling time is too long, the device may miss abrupt changes in acceleration, resulting in an inaccurate measurement of jerk.

To make a rough evaluation of the proper needed sampling time, we can examine the frequency spectral content of one of the signals coming from our simulation model. Specifically, the example taken into consideration is the acceleration behaviour of the vehicle model featuring suspensions, linkage horizontal compliance and slipping wheels (see Figure 7.1).

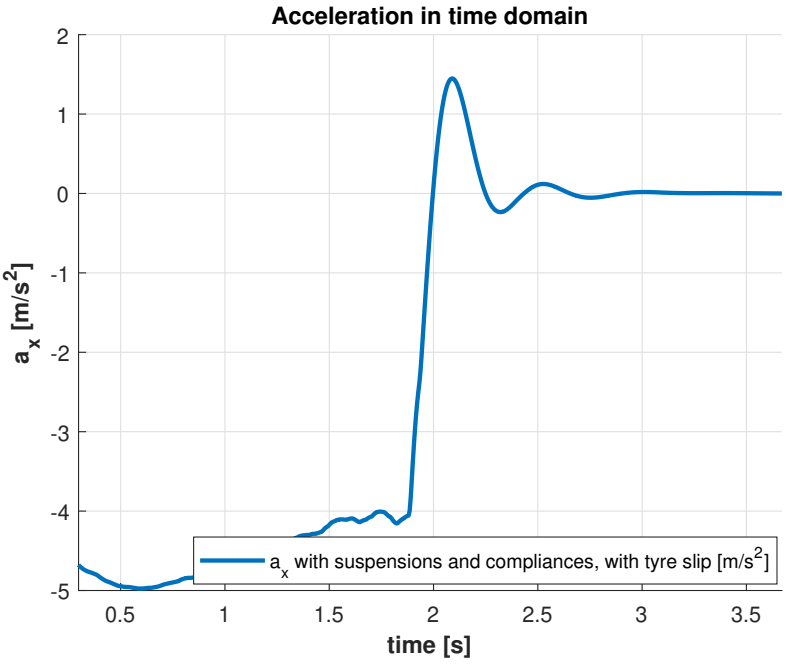

Figure 7.1: Acceleration behaviour during the braking manoeuvre of the vehicle model featuring suspensions, linkage horizontal compliance and slipping wheels.

Applying the Fourier transform to the signal we can retrieve its frequency contents. Figure 7.2 shows the single-side spectrum (up to the Nyquist frequency) of the acceleration signal illustrated in Figure 7.1. It is possible to see how after 30 [Hz] the contribution of the different components becomes very low (< -50 [dB]). These contributions are likely due to the noise originating from the input signal disturbances.

If we try to reconstruct the signal in the time domain using only the components up to 30 [Hz], the acceleration behaviour does not deviate with respect to the original one (see Figure 7.3). This indicates that sampling the signal at 30 [Hz] could provide valuable and detailed information about acceleration behaviour. However, one of the future goals to enhance this project is to actively regulate vehicle jerk. For this reason, it should be considered that for control systems, it is generally recommended to sample at a rate several times higher than the system bandwidth to ensure accurate tracking.

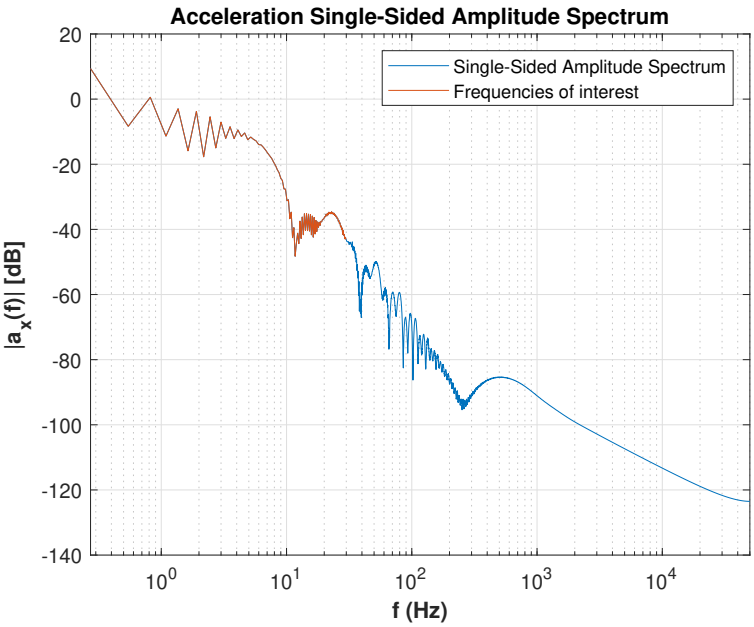

Figure 7.2: Acceleration single-side spectrum. In blue the complete acceleration spectrum. In orange the frequencies components of higher interest.

Considering the aforementioned frequency of 30 [Hz], it is advisable to opt for sensors with a sampling frequency rate around $f_s = 1$ [kHz]. These high sampling rates are achievable with very powerful, but expensive IMUs.
Another factor that affects the accuracy of jerk measurements is the resolution of the instrument or sensor. The resolution refers to the smallest detectable change in acceleration that the device can measure. A device with low resolution may not be able to capture small changes in acceleration, leading to an underestimation of jerk.

7.3 Jerk control

As mentioned in section 7.2, an important future aspect to consider is the active regulation of the vehicle jerk. Having a simulation model capable of working at very low speeds makes it possible to build and tune a controller directly in the simulation loop.

Furthermore, jerk control goes beyond the use of a dedicated controller. It is also intended as the design process aimed at guaranteeing passenger comfort, particularly

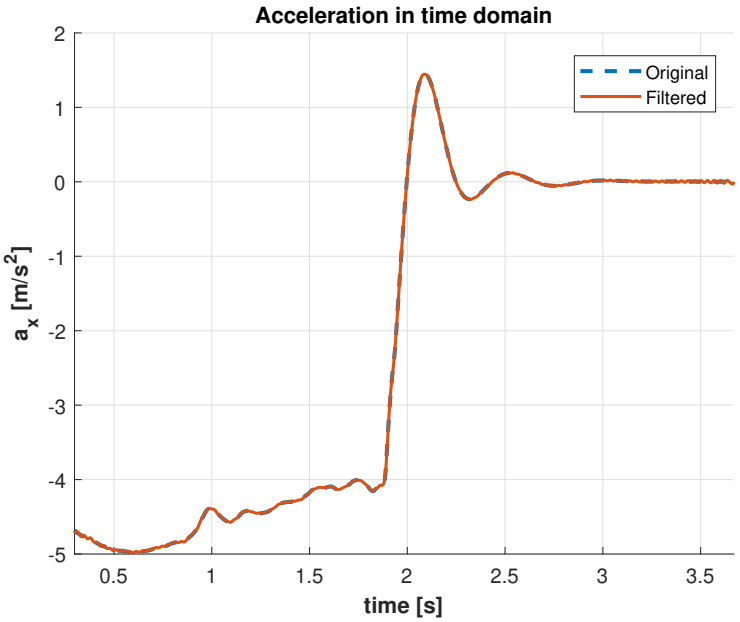

Figure 7.3: Acceleration behaviour of the vehicle during the braking manoeuvre after removing high-frequency components from the signal.

when designing suspensions and compliance elements of the vehicle. Two possible aspects can then be considered for future works:

1. Design of the suspension systems and the compliance attachment elements to minimize vehicle jerk. Active suspension is likely a key factor in achieving this goal. It is worth noting that comfort and safety are not only dependent on longitudinal dynamics. The suspension design should consider various aspects, including longitudinal and vertical dynamics, as well as vehicle performance and safety.
2. Active jerk controller. Meaning the design of specific controllers that can help to prevent or limit sudden changes in acceleration. Various approaches can be employed to achieve this goal. For instance, one possibility is to introduce an active brake pressure reducer that decreases the brake line pressure as the vehicle approaches zero speed.

However, the successful implementation of a control strategy in an actual vehicle relies on the availability of precise measurements or estimations of the vehicle states. For example, the use of controllers based on longitudinal vehicle acceleration, which is closely linked to the discomfort caused by jerk, is not commonly observed in the existing literature. The limited adoption of such controllers can be attributed to the difficulties involved in accurately measuring longitudinal acceleration in production vehicles. Typically, longitudinal acceleration is obtained from an inertial measurement unit, which is affected by signal noise [1].

Chapter 8

Conclusions and remarks

This project has provided valuable insights into the current limits of the most commonly used models for friction and tyres. It has been pointed out how non-linear dynamics models are necessary to capture the effects that arise when driving at very low speeds.

Different approaches have been evaluated for brake friction modelling. However, the flexibility of bristle models, which do not require knowledge about the state of dynamic systems, makes them suitable for vehicle simulation purposes.

An adapted LuGre friction model has been also implemented to model the tyre-ground force behaviour. The model relies on the physical background of how the tread of a tyre deforms when a force (or a torque) is applied to the wheel. However, the LuGre tyre model fails to mimic a realistic tread deformation, despite producing accurate results for the output bristle forces. Furthermore, a speed-dependency behaviour has been pointed out in section 4.2.4. Experimental evidence is still required to confirm the accuracy of the results obtained from the model. Nevertheless, it seems reasonable to integrate this speed dependency into a suitable tyre model.

A complete longitudinal vehicle model featuring the aforementioned brake and tyre friction models has been developed. Moreover, different vehicle modelling complexities have been considered to better understand the source of sudden acceleration changes. Experimental data and results have been used as a benchmark for the analysis of the vehicle models simulations, leading to noteworthy conclusions:

- When introducing vehicle attachment compliance and suspension in the model, the tyre model has minimal influence on the acceleration behaviour compared to a non-slipping wheel model. However, the use of an accurate tyre model enhances the dynamic simulation results, better reproducing the real-world behaviour of the vehicle.
- Rigid vehicle models fail to accurately represent acceleration oscillations.
- Although the inclusion of suspension models does not significantly improve the longitudinal behaviour of the models, the introduction of suspension attachment compliance allows the model to reflect experimental results.

- Incorporating tyre sidewall compliance introduces a slight deviation in the simulation outputs compared to a rigid tyre carcass. Precise knowledge of stiffness and damping values is crucial in this regard as they have a direct impact on acceleration behavior.

Suggestions about how to measure and capture jerk for comfort and safety control purposes have been provided in section 7.2 and section 7.3. Moving forward, the next steps involve the development of methods to effectively measure and control jerk. However, quantifying jerk in real-world scenarios, where sensors have finite sample rates, is a challenging task. Additionally, the implementation of control strategies that aim to achieve optimal management of jerk must rely on vehicle state measurements. Nevertheless, the availability of a simulation tool capable of accurately depicting real-world situations, even at low speeds, enables the formulation of offline strategies that can be tested in practical environments.

Bibliography

[1] Andrea Bisoffi, Francesco Biral, Mauro Da Lio, and Luca Zaccarian. "Longitudinal Jerk Estimation of Driver Intentions for Advanced Driver Assistance Systems". In: *IEEE/ASME Transactions on Mechatronics* 22.4 (2017), pp. 1531–1541. DOI: 10.1109/TMECH.2017.2716838.

[2] Juan Cabrera, Antonio Ortiz, A Simón, Francisco García, A Pérez, and Ana Perez-Blanca. "A Versatile Flat Track Tire Testing Machine A Versatile Flat Track Tire Testing Machine". In: *Vehicle System Dynamics* 40 (2003), pp. 271–284. DOI: 10.1076/vesd.40.2.271.16542.

[3] Xunjie Chen, Jingang Yi, Junyu Qian, and Hao Wang. "An Integrated Tread Beam/LuGre Tire-Road Friction Model". In: *IFAC-PapersOnLine* 55 (2022), pp. 688–693. DOI: 10.1016/j.ifacol.2022.11.262.

[4] Joško Deur. "Modeling and Analysis of Longitudinal Tire Dynamics Based on the Lugre Friction Model". In: *IFAC Proceedings Volumes* 34.1 (2001), pp. 91–96. DOI: 10.1016/S1474-6670(17)34383-5.

[5] P. Dupont, Armstrong B., and V. Hayward. "Elasto-plastic friction model: contact compliance and stiction". In: *Proceedings of the 2000 American Control Conference. ACC (IEEE Cat. No.00CH36334)* 2 (2000), pp. 1072–1077. DOI: 10.1109/ACC.2000.876665.

[6] N. Fuhg Jan and Amélie Fau. "Surrogate model approach for investigating the stability of a friction-induced oscillator of Duffing's type". In: *Nonlinear Dynamics* 98 (2019), pp. 1709–1729. DOI: 10.1007/s11071-019-05281-2.

[7] Bengt J H Jacobson, Mats Jonasson, and Fredrik Bruzelius. *Compendium in vehicle motion engineering*. Chalmers University of Technology, 2022.

[8] Samuel Jung, Tae-Yun Kim, and Wan-Suk Yoo. "Advanced slip ratio for ensuring numerical stability of low-speed driving simulation. Part I: Longitudinal slip ratio". In: *Proceedings of the Institution of Mechanical Engineers, Part D: Journal of Automobile Engineering* 233.8 (2019), pp. 2000–2006. DOI: 10.1177/0954407018759738.

[9] Wei Linag, Jure Medanic, and Roland Ruhl. "Analytical dynamic tire model". In: *Vehicle System Dynamics* 46.3 (2008), pp. 197–227. DOI: 10.1080/00423110701267466.

[10] Alberto López, José Luis Olazagoitia, Francisco Marzal, and María Rosario Rubio. "Optimal parameter estimation in semi-empirical tire models". In: *Automobile Engineering* 233 (2018), pp. 73–87. DOI: 10 . 1177 / 0954407018779851.

[11] Filipe Marques, Paulo Flores, Claro J. C. Pimenta, and Hamid M. Lankarani. "A survey and comparison of several friction force models for dynamic analysis of multibody mechanical systems". In: *Nonlinear Dynamics* 86 (2016), pp. 1407–1443. DOI: 10.1007/s11071-016-2999-3.

[12] Alexander O'Neill, Jan Prins, John F Watts, and Patrick Gruber. "Enhancing brush tyre model accuracy through friction measurements". In: *Vehicle System Dynamics* 60 (2022), pp. 2075–2097. DOI: 10.1080/00423114.2021.1893766.

[13] Hans B. Pacejka and Igo J.M. Besselink. *Tire and vehicle dynamics*. Elsevier Science & Technology, 2012. ISBN: 9780080970172.

[14] Ettore Pennestri, Valerio Rossi, Pietro Salvinia, and Valentini Pier Paolo. "Review and comparison of dry friction force models". In: *Nonlinear Dynamics* 83 (2016), pp. 1785–1801. DOI: 10.1007/s11071-015-2485-3.

[15] James R. Phillips. "A Longitudinal Slip Tire Model for Brake Control Systems: Features and Uses in Simulation, Control Synthesis and Stability Analysis". In: *SAE Transactions* 111 (2002), pp. 507–515. DOI: 10.4271/2002-01-2949.

[16] Luigi Romano, Fredrik Bruzelius, and Bengt Jacobson. "An extended LuGre-brush tyre model for large camber angles and turning speeds". In: *Vehicle System Dynamics* (2022), pp. 1–33. DOI: 10.1080/00423114.2022.2086887.

[17] Panagiotis Tsiotras, Efstathios Velenis, and Michel Sorine. "A LuGre Tire Friction Model With Exact Aggregate Dynamics". In: *Vehicle System Dynamics* 42 (2004), pp. 195–210. DOI: 10.1080/00423110412331289835.

Appendix A

LuGre tyre model - contact patch coordinate derivative

In this appendix, analytical solutions are provided for the term $\frac{\partial \xi}{\partial t} = |\omega \cdot R_w|$ presented in section 4.2.1. Let us consider the tyre model of Figure A.1. The contact patch can be considered flatten to the ground by the weight of the vehicle. the contact patch coordinate ξ moves from 0 to L and we can consider that, in those two points, the tyre radius is equal to the undeformed radius R_w.

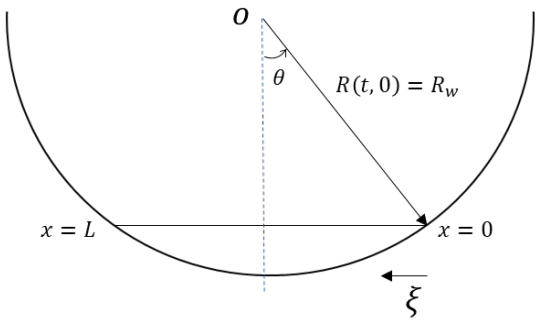

Figure A.1: LuGre tyre model - contact patch geometry.

Considering the angle θ going from θ_{max} to $-\theta_{max}$, it is possible to write down the following geometrical equations

$$R_w \cdot \sin(\theta_{max}) = \frac{L}{2}, \tag{A.1a}$$

$$R(\theta) = R_w \cdot \cos(\theta_{max} - |\theta|), \tag{A.1b}$$

$$\xi = \frac{L}{2} - R(\theta) \cdot \sin(\theta), \quad \theta \, \epsilon \, [-\theta_{max}, \theta_{max}]. \tag{A.1c}$$

At this point, the derivative $\frac{\partial \xi}{\partial t}$ becomes

$$\frac{\partial \xi}{\partial t} = \frac{\partial \left[\frac{L}{2} - R(\theta) \cdot \sin(\theta)\right]}{\partial t} = -\frac{\partial [R(\theta)]}{\partial t} \cdot \sin(\theta) - R(\theta) \cdot \frac{\partial [\sin(\theta)]}{\partial t}$$

$$= -\frac{\partial[R_w \cdot \cos(\theta_{max} - |\theta|)|]}{\partial t} \cdot \sin(\theta) - [R_w \cdot \cos(\theta_{max} - |\theta|)] \cdot \frac{\partial[\sin(\theta)]}{\partial t}$$

$$= R_w \cdot \sin(\theta_{max} - |\theta|) \cdot (-|\dot{\theta}|) \cdot \sin(\theta) - R_w \cdot \cos(\theta_{max} - |\theta|) \cdot \cos(\theta) \cdot \dot{\theta}. \tag{A.2}$$

Considering that θ is decreasing passing from $\xi = 0$ to $\xi = L$, the derivative $\dot{\theta}$ can be written as

$$\dot{\theta} = -|\omega| \tag{A.3}$$

and so (A.2) becomes

$$|\omega \cdot R_w| \cdot [\pm \sin(\theta_{max} - |\theta|) \cdot \sin(\theta) + \cos(\theta_{max} - |\theta|) \cdot \cos(\theta)],$$

with the $+$ sign that holds for positive θ angles and the $-$ for negative ones. To understand the weight of the multiplicative term

$$m_t = \pm \sin(\theta_{max} - |\theta|) \cdot \sin(\theta) + \cos(\theta_{max} - |\theta|) \cdot \cos(\theta), \tag{A.4}$$

let us consider an extreme case where a wheel with a radius $R_w = 0.3$ $[m]$ has a contact patch with a length $L = 0.3$ $[m]$ (clearly this value is very large for road cars where it is normally around 0.1 $[m]$). From (A.1):

$$\theta_{max} = 0.5236 \ \ [m]$$

and (A.4) has the shape as in (A.2).

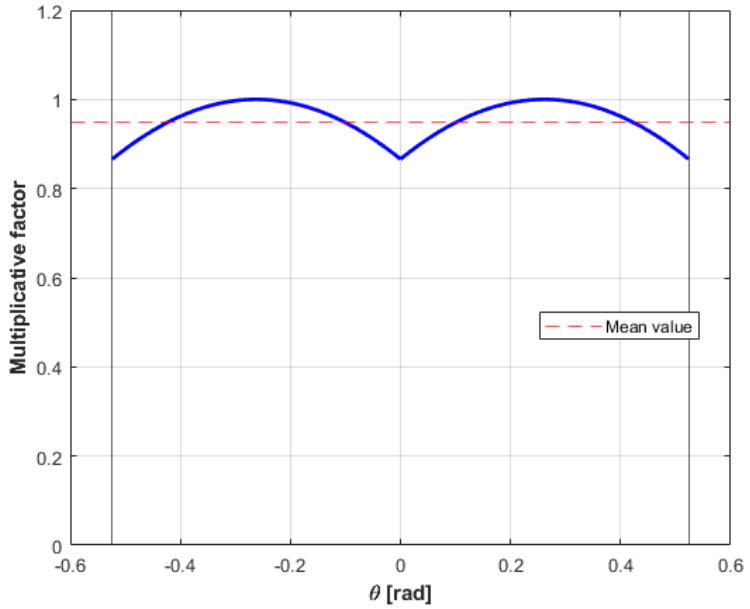

Figure A.2: Wheel rim speed - multiplicative term with $L = 0.3$ $[m]$.

It can be notice how the mean value ($\tilde{m}_t$) of Equation A.1 is roughly 0.9540 and always above 0.9, with

$$\tilde{m}_t = \frac{\int_{-\theta_{max}}^{\theta_{max}} [\pm \sin(\theta_{max} - |\theta|) \cdot \sin(\theta) + \cos(\theta_{max} - |\theta|) \cdot \cos(\theta)]}{2 \cdot \theta_{max}} = 0.9540.$$

Considering all the assumptions behind the model and the big contact patch length used, we can state that the term $\frac{\partial \xi}{\partial t}$ can be approximated quite well as

$$\frac{\partial \xi}{\partial t} \cong |\omega \cdot R_w|. \tag{A.5}$$

Note that for $L = 0.1$ $[m]$ we have

$$\theta_{max} = 0.1674 \ \ [m],$$

$$\tilde{m}_t = 0.9952.$$

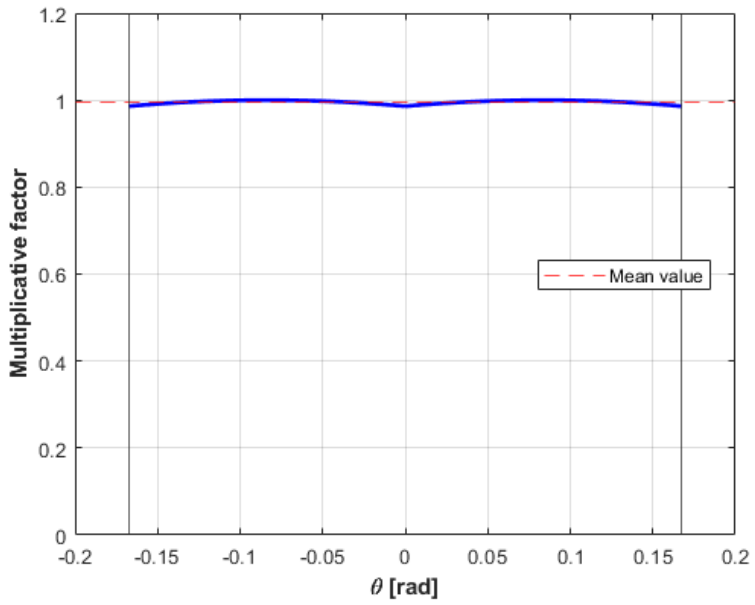

Figure A.3: Wheel rim speed - multiplicative term with $L = 0.1$ $[m]$.

Appendix B

Premium SUV - Parameters

The following is the list of the vehicle parameters used for the mathematical-physical representation of longitudinal vehicle models.

B.1 Vehicle's body parameters

Parameter	Unit of measure	Value	Description
m_s	[kg]	1804	Sprung mass
$m_{u,f}$	[kg]	130	Front unsprung mass
$m_{u,r}$	[kg]	144	Rear unsprung mass
$J_{s,y}$	[kg·m^2]	3876	Pitching inertia
l_f	[m]	1492	Front axle - CoG distance
l_r	[m]	1492	Rear axle - CoG distance
h_G	[m]	0.673	Overall CoG height
$h_{G,s}$	[m]	0.730	Sprung mass CoG height
h_{Aer}	[m]	0.888	Aerodynamics pressure center height
A_f	[m^2]	3.248	Vehicle frontal area
C_x	[-]	0.28	Aerodynamics drag coefficient

B.2 Vehicle's suspension values

Parameter	Unit of measure	Value	Description
$c_{sus,f}$	[N/m]	$25{\cdot}10^3$	Single front suspension stiffness
$d_{sus,f}$	[Ns/m]	$3.75{\cdot}10^3$	Single front suspension damping
$c_{sus,r}$	[N/m]	$30{\cdot}10^3$	Single rear suspension stiffness
$d_{sus,r}$	[Ns/m]	$4.50{\cdot}10^3$	Single rear suspension damping
$c_{sus,h}$	[N/m]	$200{\cdot}10^3$	Attachment compliance stiffness[1]
$d_{sus,h}$	[Ns/m]	$7{\cdot}10^3$	Attachment compliance damping[2]

B.3 Vehicle's brakes parameters

Parameter	Unit of measure	Value	Description
R_m	[m]	0.2	Brake disc average radius
$\mu_{s,b}$	[-]	0.7	Static disc-pad friction coefficient
$\mu_{d,b}$	[-]	0.3	Dynamic disc-pad friction coefficient
N_f	[-]	4	Number of front brake pistons
N_r	[-]	2	Number of rear brake pistons
A_p	[m^2]	0.001	Brake pad pistons area
	LuGre model parameters		
$\sigma_{0,b}$	[1/m]	5.65	Bristles' stiffness
$\sigma_{1,b}$	[s/m]	2.38	Bristles' damping
$\sigma_{2,b}$	[s/m]	0	Viscous coefficient
$v_{s,b}$	[m/s]	0.035	Stribeck velocity
α_b	[-]	2	Shape factor

[1] Same value for front and rear tyres.
[2] Same value for front and rear tyres.

B.4 Vehicle's tyres parameters

Parameter	Unit of measure	Value	Description
R_c	[m]	0.3695	Wheel loaded radius
K	[s^2/m^2]	$2.6 \cdot 10^{-8}$	Speed to Rolling resistance coefficient
$J_{rim,f}$	[$kg \cdot m^2$]	1.573	Front single wheel rim inertia
$J_{rim,r}$	[$kg \cdot m^2$]	1.544	Rear single wheel rim inertia
$J_{belt,f}$	[$kg \cdot m^2$]	0.175	Front single wheel belt inertia
$J_{belt,r}$	[$kg \cdot m^2$]	0.172	Rear single wheel belt inertia[3]
c_{belt}	[Nm/rad]	$4 \cdot 10^4$	Sidewall stiffness[4]
d_{belt}	[Nms/rad]	$2 \cdot 10^3$	Sidewall damping[5]
LuGre model parameters			
L	[m]	0.1	Contact patch length
N	[-]	100	Number of bristles
$\mu_{s,t}$	[-]	1.95	Static friction coefficient
$\mu_{d,t}$	[-]	0.73	Dynamic friction coefficient
σ_0	[1/m]	650	Bristles' stiffness
σ_1	[s/m]	2	Bristles' damping
σ_2	[s/m]	0	Viscous coefficient
$v_{s,t}$	[m/s]	3.2	Stribeck velocity
α_t	[-]	0.42	Shape factor

[3] If the compliance of the wheel sidewall is not considered, the rim and the belt inertia are summed together.

[4] Same value for front and rear tyres.

[5] Same value for front and rear tyres.

DEPARTMENT OF MECHANICS AND MARITIME SCIENCES
CHALMERS UNIVERSITY OF TECHNOLOGY
Gothenburg, Sweden
www.chalmers.se

CHALMERS
UNIVERSITY OF TECHNOLOGY